ANNUAL REVIEWS

Annual Review of Earth and Planetary Sciences

Heterogeneity of Seismic Wave Velocity in Earth's Mantle

Jeroen Ritsema[1] and Vedran Lekić[2]

[1]Department of Earth and Environmental Sciences, University of Michigan, Ann Arbor, Michigan 48109, USA; email: jritsema@umich.edu

[2]Department of Geology, University of Maryland, College Park, Maryland 20742, USA; email: ved@umd.edu

Annu. Rev. Earth Planet. Sci. 2020. 48:377–401

First published as a Review in Advance on February 4, 2020

The *Annual Review of Earth and Planetary Sciences* is online at earth.annualreviews.org

https://doi.org/10.1146/annurev-earth-082119-065909

Keywords

seismology, deep mantle, tomography, geodynamics

Abstract

Seismology provides important constraints on the structure and dynamics of the deep mantle. Computational and methodological advances in the past two decades improved tomographic imaging of the mantle and revealed the fine-scale structure of plumes ascending from the core-mantle boundary region and slabs of oceanic lithosphere sinking into the lower mantle. We discuss the modeling aspects of global tomography including theoretical approximations, data selection, and model fidelity and resolution. Using spectral, principal component, and cluster analyses, we highlight the robust patterns of seismic heterogeneity, which inform us of flow in the mantle, the history of plate motions, and potential compositionally distinct reservoirs. In closing, we emphasize that data mining of vast collections of seismic waveforms and new data from distributed acoustic sensing, autonomous hydrophones, ocean-bottom seismometers, and correlation-based techniques will boost the development of the next generation of global models of density, seismic velocity, and attenuation.

- Seismic tomography reveals the 100-km to 1,000-km scale variation of seismic velocity heterogeneity in the mantle.
- Tomographic images are the most important geophysical constraints on mantle circulation and evolution.

INTRODUCTION

Variations in temperature, composition, grain size, and volatile distribution within Earth's deep interior are causally related to planetary processes including plate tectonics, continental breakup, mantle convection, hotspot volcanism, and the water and carbon cycles crucial for maintaining long-term habitability of the surface environment. As such, mapping them informs our understanding of planetary dynamics and offers insights into Earth's geological past. Seismology provides the strongest global constraints on these variations through their effects on rigidity, compressibility, anelasticity, density, and anisotropy of mantle materials.

The first global-scale maps of shear-velocity (V_S) and compressional wave (V_P) variations in the mantle (e.g., Dziewoński et al. 1977, Woodhouse & Dziewoński 1984) made clear that plate tectonics is intimately linked to dynamic processes in the deep interior. The steady progress in global-scale seismology and seismic tomography during the next 35 to 40 years must be attributed to the expansion of networks of broadband seismometers, the open-access availability of seismic data, and increased computer power that have enabled seismologists to use millions of seismograms in their analyses. Current seismic studies explore diverse seismic phases across the full band of seismic frequencies, and they are based on numerical methods and theories of wave propagation with few approximations.

The literature on seismic studies of velocity heterogeneity in Earth's mantle and multidisciplinary research of deep Earth structure and dynamics is vast and diverse. It is therefore inevitable that a review paper is incomplete and selective. We have chosen to focus our discussion on recent progress in global-scale seismic imaging of the mantle roughly from the 660-km phase transition at the base of the mantle transition zone (MTZ) to the core-mantle boundary (CMB) at a depth of 2,891 km. We start with an overview of the state of the art in seismic tomography, identify consistently imaged structures and patterns of mantle seismic heterogeneity, and describe in some detail how seismic imaging has influenced research on the nature and evolution of compositional heterogeneity in the deep mantle, the formation of focused upwellings (i.e., plumes), and the fate of subducted slabs of oceanic lithosphere. We close with a discussion of open questions and promising research directions.

EARTH'S LARGE-SCALE SEISMIC STRUCTURE FROM SEISMIC TOMOGRAPHY

Spherically Symmetric Structure

Even in an article on the three-dimensional (3D) structure of the mantle, it is useful to establish that, to first order, Earth properties depend primarily on radius. Density and both V_P and V_S increase from the Moho (i.e., the boundary between the crust and mantle) to the CMB by about 70%. Strong vertical gradients and discontinuities in the MTZ and possibly hundreds of kilometers above the CMB (i.e., the top of D″) are produced by phase transitions of major minerals in mantle rock. However, lateral variations of wavespeeds and density do not exceed a few percent except in the uppermost and lowermost mantle.

Figure 1 shows stacks of about a million seismograms from globally distributed stations and earthquakes. It brings out high-amplitude vertically and horizontally polarized waves. The signals line up along sharp travel-time curves, which demonstrates that seismic waves with long propagation paths are recorded with little travel-time variation. Along with free-oscillation frequencies and astrometric data, these travel-time curves form the basis for spherically symmetric (i.e., 1D) reference models such as the Preliminary Reference Earth Model (Dziewoński & Anderson 1981). The dominance of depth variations makes it possible to identify many specific arrivals

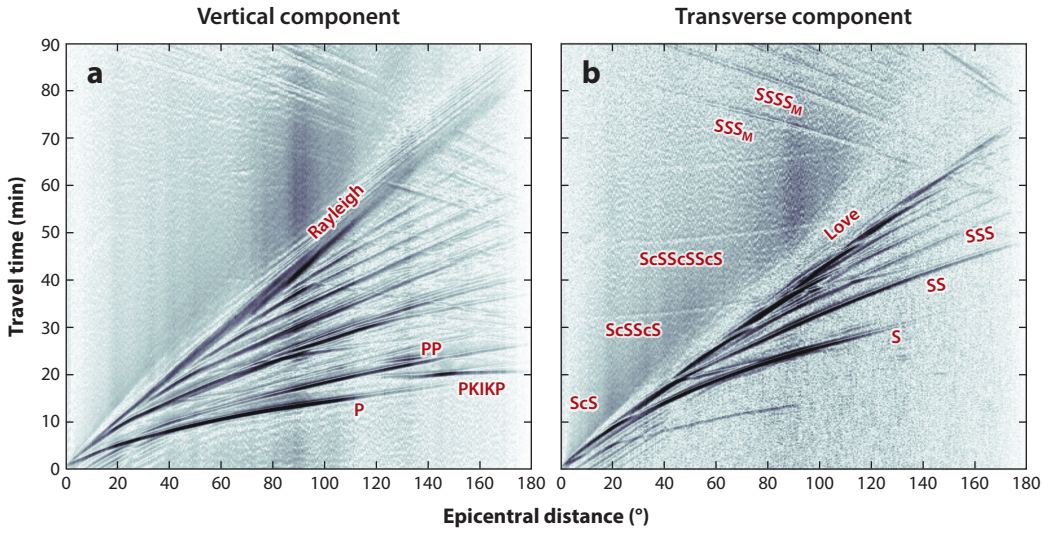

Figure 1

Stacks of globally recorded seismograms using short- to long-term averages for vertical (panel *a*) and transverse (panel *b*) component waveforms generated by shallow earthquakes between 1990 and 2012. The waveforms have been low-pass filtered at 0.1 Hz. Several high-amplitude phases are labeled in red. The stacks were produced by Dr. Alexander Hutko at the IRIS Data Management Center (IRIS DMC 2014). Subscript M denotes waves propagating along the major arc from source to receiver.

in teleseismic (epicentral distance >25°) waveforms and to use them for tomographic mapping of the 3D structure. Except along a few highly anomalous paths, ray-theoretical predictions of onset times of all body-wave phases based on 1D models are accurate to within several seconds, and waveforms computed using normal-mode theory or direct solution methods reproduce the recorded waveforms accurately at long periods. Recent reassessments of global 1D models incorporating new data and inversion techniques have confirmed many of the characteristics of 1D models. However, they also proposed refinements to, for example, the radius of the inner core, average velocities at the base of the mantle, the depth dependence of attenuation (e.g., de Wit et al. 2014), velocity gradients at the top of the outer core (e.g., Irving et al. 2018, Kaneshima 2018), and the global significance of the 220-km discontinuity (e.g., Kustowski et al. 2008).

Data Types

To first order, the choice in data types determines where in the mantle tomographic models optimally resolve seismic structure. Models derived solely from the travel-time delays of teleseismic body waves (e.g., Zhao 2004, Li et al. 2008, Obayashi et al. 2013) constrain vertical variations of seismic structure in the upper third or quarter of the mantle (<700–1,000 km) poorly because teleseismic body waves traverse the depth range nearly vertically. However, travel-time models can delineate fine-scale structure in the upper mantle of subduction zones, where earthquakes are dispersed over a broad depth range, and in regions where dense seismic networks have been deployed or when triplicated waves turning in the upper mantle have been included.

Tomographic models based purely on fundamental-mode surface waves (e.g., Shapiro & Ritzwoller 2002, Zhou et al. 2006) do not resolve seismic structure in the deep mantle (>350 km) but provide excellent constraints on upper-mantle structure especially in the oceanic regions where few stations have been deployed. Models that incorporate overtone data resolve structure in the transition zone and uppermost lower mantle (e.g., Visser et al. 2008, Debayle &

Ricard 2012, Schaeffer & Lebedev 2013, Ho et al. 2016). Models based on combinations of body-wave and surface-wave data (e.g., Houser et al. 2008, Kustowski et al. 2008, Auer et al. 2014, Chang et al. 2015), normal-mode and surface-wave data (e.g., Trampert et al. 2004), or all of these three data types (e.g., Ritsema et al. 2011, Moulik & Ekström 2014, Durand et al. 2017) provide more uniform coverage. Models derived from full waveforms include additional portions of seismograms that need not be associated with standard seismic phases (e.g., French & Romanowicz 2014, Bozdağ et al. 2016). Finally, the GyPSuM models by Simmons et al. (2010) incorporate free-air gravity, plate motions, excess ellipticity of the CMB, the nonisostatic topography of Earth's surface, and mineral-physics relationships as additional constraints in a tomographic inversion using body-wave travel-time data.

Theoretical Treatment

All seismic tomography is built upon finding a model, **m**, of Earth's seismic structure that minimizes the misfit between the phases and/or amplitudes of observed seismic waves, **d**, and those predicted by the model, **g**(**m**). This inverse problem has been tackled in a variety of ways, either by model space search approaches (Mosegaard & Tarantola 1995) or by linearization around a starting model, which can be iterated on to account for nonlinearity inherent in **g**(**m**) (e.g., Tarantola 2005). Model space searches can be accomplished by the repeated solution of the forward problem, which predicts the amplitudes and/or phases of seismic waves for a given model of Earth's interior. The forward problem can be solved accurately using numerical methods, including the spectral element method (e.g., Komatitsch & Tromp 2002, Leng et al. 2019). However, high computational cost makes numerical methods ill-suited for model space search approaches and for modeling high-frequency signals. Therefore, seismologists continue to rely on approximate methods based on ray or perturbation theory. Tomographic methods based on (iterative) linearization require as few as a single solution of the forward problem at the cost of having to evaluate the Fréchet derivatives that relate model perturbations $\delta\mathbf{m}$ to perturbations in the data $\delta\mathbf{d}$.

The amplitude and phase of seismic waves depend on the elastic and anelastic properties in a finite volume. This volume is often represented by a Fresnel zone defined as a region in which singly scattered waves arrive within a specific time after the direct wave. For travel times, this threshold time is either a half or a quarter of the wave dominant period when the measurements are made using cross correlation or by identifying the onset, respectively (Gudmundsson 1996). Ray theory is an infinite-frequency approximation in which energy is assumed to travel along infinitesimally thin ray paths for body waves and beneath great-circle paths for surface waves. While it is valid for high-frequency onset times, ray theory becomes inaccurate when Fresnel zones are similar in size to seismic heterogeneities (e.g., Spetzler & Snieder 2001). This places a limit on the resolution of fine-scale structure. The limitations of ray theory motivated the development of Born scattering theory to describe more accurately the finite-frequency sensitivity of travel times (e.g., Snieder 1986, Marquering & Snieder 1995, Tanimoto 1995, Dahlen et al. 2000) and waveforms (e.g., Li & Romanowicz 1995, Marquering et al. 1998). Earlier efforts often restricted the evaluation of Born scattering to the 2D vertical planes defined by the great-circle arc (e.g., Li & Romanowicz 1996). Romanowicz et al. (2008) discuss the consequences of this approximation on accuracy.

By the 2000s, computational resources became large enough to relax the 2D approximation and compute Fréchet derivatives called 3D finite-frequency kernels or banana-doughnut kernels, inspired by the shape and cross-sectional form of these culinary chimera. These 3D finite-frequency kernels are calculated within a background 1D model using the paraxial approximation (e.g., Dahlen et al. 2000) or within a fully 3D model using adjoint methods (e.g., Tromp et al. 2005). Born theory itself has limitations, namely that the phase perturbation to the seismic wave

is small (e.g., Marquering et al. 1998, Panning et al. 2009). Methods based on the Rytov approximation or hybrid methods such as the nonlinear asymptotic coupling theory (Li & Romanowicz 1995) may be more appropriate for estimating weak velocity perturbations of large spatial extent.

Several global tomographic models have pioneered the use of either 3D finite-frequency kernels—such as the PRI-S05, PRI-P05 (Montelli et al. 2004, 2006), and SH18CE (Takeuchi 2007) models—or accurate forward modeling based on the spectral element method—such as the upper-mantle SEMum (Lekić & Romanowicz 2011) and whole-mantle SEMUCB-WM1 (French & Romanowicz 2014) models. Model GLAD-M15 (Bozdağ et al. 2016) is based on waveform kernels computed using adjoint methods. The costs associated with accurately computing 3D waveforms and sensitivity kernels necessitate the use of smaller data sets. For example, model GLAD-M15 is based on a data set of 253 earthquakes, a factor of 20 smaller than ray-based tomographic models. Since the model estimation updates went through 15 iterations, GLAD-M15 has not yet moved significantly from its starting model S362ANI (Kustowski et al. 2008), although slab and plume structures in the mantle appear better defined. The promise of global-scale adjoint tomography to accurately resolve strong wavespeed contrast and fine-scale structure in the crust and upper mantle is evident from adjoint tomography on regional (<500 km) (Tape et al. 2009) and continental scales (e.g., Fichtner et al. 2009, Zhu et al. 2012, Krischer et al. 2018).

Tomographic models differ from one another not only in the evaluation of the forward problem and the Fréchet derivatives but also in how the problem is linearized, the model **m** is parameterized, and prior assumptions (e.g., the structure of the crust) and model smoothness (i.e., explicit regularization) are incorporated. Most tomographic models have been constructed by fully linearizing the inverse problem (e.g., Ritsema et al. 2011), although those based on waveform fitting often rely on iterative methods such as conjugate gradient descent (e.g., Bozdağ et al. 2016) or a quasi-Newton method (e.g., French & Romanowicz 2014). Choices of parameterization on inversion can be consequential (e.g., Trampert & Snieder 1996), particularly for poorly resolved parameters such as radial anisotropy (e.g., Gao & Lekić 2018). Similarly, assumptions about crustal structure can significantly affect tomographic models of radial anisotropy (e.g., Panning et al. 2010, Chang & Ferreira 2017). Finally, regularization choices are particularly impactful on the retrieval of amplitudes (e.g., Burdick & Lekić 2017) of velocity variations.

Resolution Analysis

To test hypotheses about conditions and processes in the deep interior, model uncertainty and trade-offs must be quantified. Traditionally, this has been accomplished by computing the resolution operator, R, and/or the posterior model covariance matrix, $\hat{C}_M$ (see Tarantola 2005), which describe spurious elongation and weakening of imaged velocity anomalies due to model parameterization, data processing and weighting, and model regularization (i.e., a priori constraints on model smoothness and amplitudes). It is not straightforward to interpret R and $\hat{C}_M$ directly because the number of model parameters is large. Commonly used tests are so-called point-spread functions (PSFs) or checkerboard tests. Here, R is applied to a single-parameter spike or to a pattern of alternating velocity anomalies, respectively, to determine how that structure would appear in the tomographic model. Checkerboard tests can be misleading because checkerboards represent only a single wavelength of heterogeneity (e.g., Rawlinson & Spakman 2016). The visualization of PSFs is therefore preferred.

In **Figure 2*a*** we show the vertical forms of PSFs beneath Iceland at depths of 125, 600, 950, and 1,450 km computed using R for tomographic model S20RTS. The PSFs are widest in the MTZ because the wave type that primarily constrains the MTZ (i.e., overtone Rayleigh waves in the case of S20RTS) is sensitive to shear-velocity structure within a relatively broad depth range.

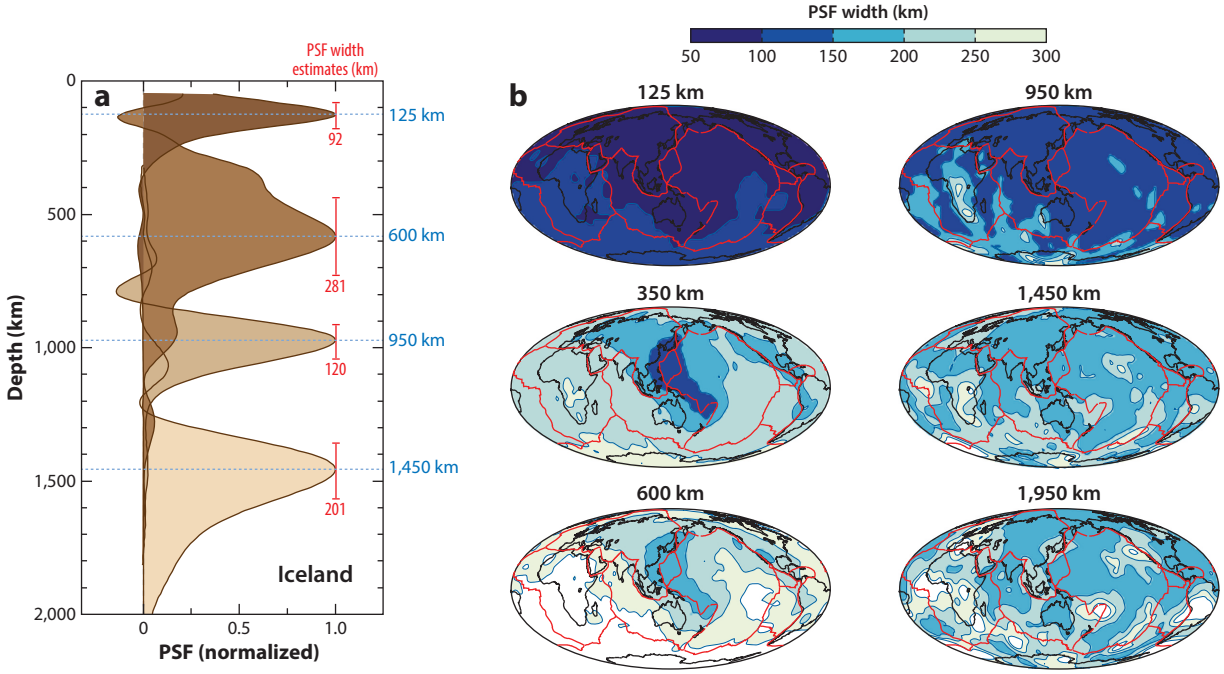

Figure 2

(*a*) Vertical cross sections through point-spread functions (PSFs) calculated for model S20RTS (Ritsema et al. 1999) for depths of 125, 600, 950, and 1,450 km (from *dark* to *light brown*) beneath Iceland. The red vertical bars and values to the right represent estimates of the width of the PSF, defined by the width of the region centered at the maximum (*blue dashed lines*) that covers 50% of the area below the PSF. (*b*) Global maps of the width of the PSF (see panel *a*) at 125-, 350-, 600-, 950-, 1,450-, and 1,950-km depth.

Figure 2*b* shows estimates of the vertical extents of the PSFs for six depths in the mantle and locations around the globe. It demonstrates further that, for S20RTS, model resolution is the lowest (i.e., PSFs are widest) in the MTZ except for the western Pacific region, and that for all depths model resolution is lowest beneath Africa and regions of the Southern Hemisphere where data coverage is typically poor. Qualitatively similar trends in PSFs can be expected across global V_S models due to inherent data limitations, while the horizontal and vertical extents of PSFs are expected to be even broader in global V_P models.

Importantly, this type of uncertainty analysis fails to account for approximations made in the computations of $\mathbf{g}(\mathbf{m})$ or the Fréchet kernels and assumes that the problem can be linearized. It will typically underestimate actual uncertainties and neglect potential nonuniqueness in model parameter estimates. Since computing the complete R or $\hat{C}_M$ exactly is prohibitively expensive in waveform tomography, seismologists frequently use approximate second-derivative matrices (i.e., Hessians) (e.g., French & Romanowicz 2014) or so-called random probing to estimate spatial variations of resolution lengths and strength of parameter trade-offs (Fichtner & van Leeuwen 2015). PSFs of specific target parameters can be computed accurately in three-dimensionally heterogeneous models using adjoint methods (Fichtner & Trampert 2011). Model space search approaches can also be used to assess nonuniqueness and trade-offs in tomographic inversion (e.g., Trampert et al. 2004, Burdick & Lekić 2017), albeit by approximating the forward problem, $\mathbf{g}(\mathbf{m})$. Nevertheless, application of the realistic resolution operators when comparing predictions from geodynamical simulations against tomographic models is prudent, particularly at the smallest length scales.

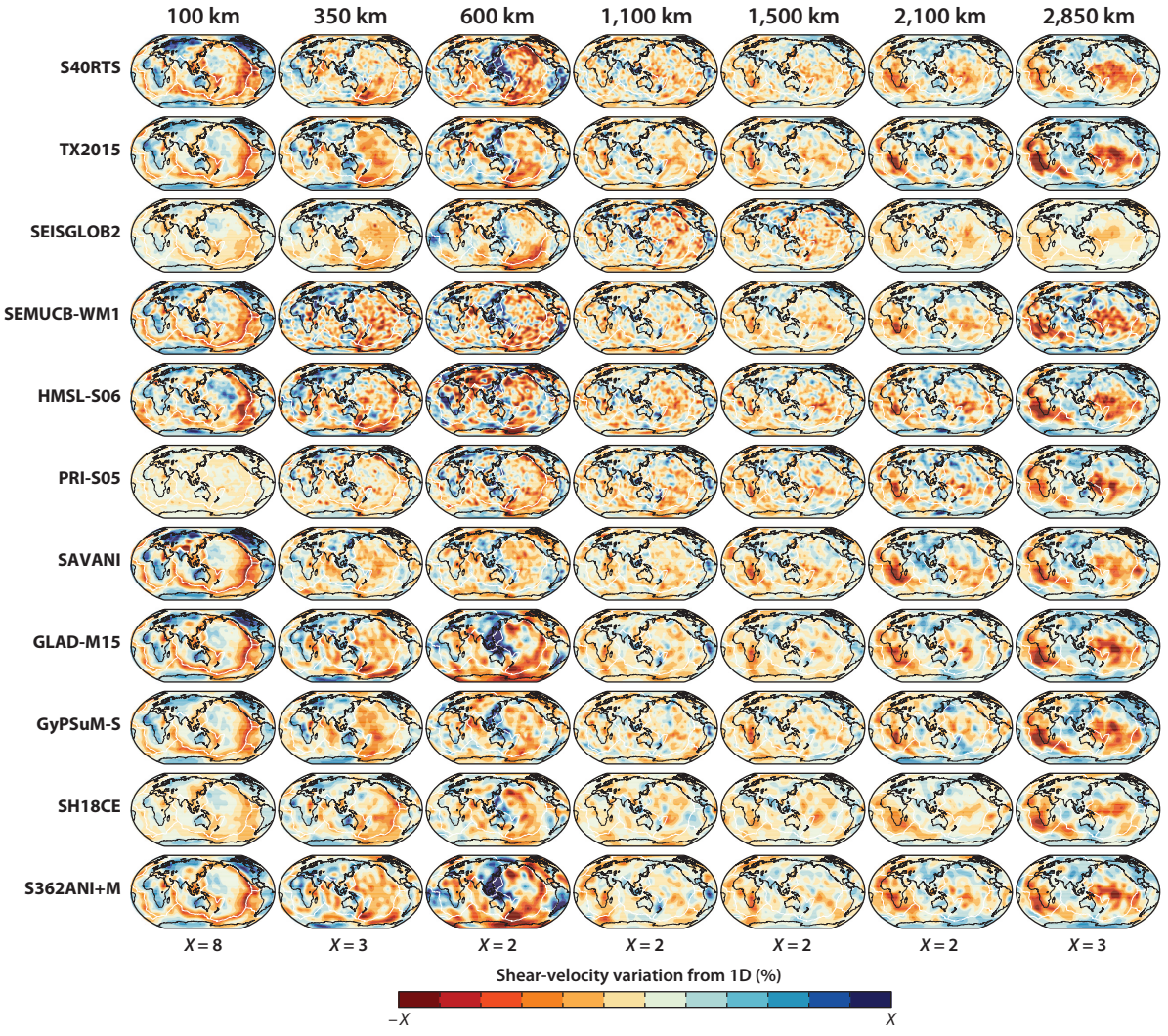

Figure 3

Maps of shear-velocity variations at depths of (from *left* to *right*) 100, 350, 600, 1,100, 1,500, 2,100, and 2,850 km according to whole-mantle models (from *top* to *bottom*) S40RTS (Ritsema et al. 2011), TX2015 (Lu & Grand 2016), SEISGLOB2 (Durand et al. 2017), SEMUCB-WM1 (French & Romanowicz 2014), HMSL-S06 (Houser et al. 2008), PRI-S05 (Montelli et al. 2006), SAVANI (Auer et al. 2014), GLAD-M15 (Bozdağ et al. 2016), GyPSuM-S (Simmons et al. 2010), SH18CE (Takeuchi 2007), and S362ANI+M (Moulik & Ekström 2014). Note that the maxima (*X*) of the depicted velocity perturbations are different for each depth.

Maps of Shear-Velocity Heterogeneity

At large scales (>2,000–5,000-km wavelength), lateral variations of seismic wavespeeds in Earth's mantle have been imaged consistently. **Figure 3** illustrates this for 11 recent V_S models, but they are also consistent in older models (e.g., Romanowicz 2003). Some of the model discrepancies originate from differences in data sets and modeling choices as discussed earlier. For example, model PRI-S05 is a teleseismic travel-time model and does not resolve the seismic structure in the upper mantle. SEISGLOB2 appears to be more strongly damped than other models, and the

structure in S40RTS is relatively small at 2,850-km depth because the splines to parameterize radial velocity variations in the lowermost mantle are relatively broad. In the following sections, we discuss key features of mantle heterogeneity using principal component, cluster, and spectral analysis.

Principal Component Analysis

Principal component analysis (PCA) helps to identify dominant features of and trends in multivariate data sets, and it has found widespread use in geochemistry and time-series analysis. Here, we apply PCA to tomography models S40RTS (Ritsema et al. 2011) and S362ANI+M (Moulik & Ekström 2014). We begin by resampling these two models every 50 km in depth and laterally on a grid of 10,242 knots that are quasi-equally distributed around the globe with an average spacing of 2°. At each depth z_k, the tomographic model is represented by a vector $\mathbf{v}_i$ whose elements are the model values at knot locations (θ_i, φ_i). At this point, we estimate a mantle shear-velocity (dV_S/V_S) structure covariance matrix C_{jk}, whose values are given by the dot product between vectors $\mathbf{v}$ corresponding to depths z_k and z_j—that is, $C_{jk} = \sum_i \mathbf{v}_i(z_j)\mathbf{v}_i(z_k)$. The diagonal elements of C_{jk} are the variance of dV_S/V_S variations at each depth. The off-diagonal elements describe how structure covaries between different pairs of depths; large positive (negative) values correspond to highly (anti)correlated structure, and values near zero indicate that the pattern of dV_S/V_S between those depths is dissimilar. When normalized by the product of standard deviations of vectors $\mathbf{v^k}$ and $\mathbf{v^j}$, matrix C_{jk} is sometimes referred to as the radial correlation function. Because C_{jk} is real and symmetric by construction, its eigenvectors are orthogonal and its eigenvalues are real. It can be diagonalized as $\mathrm{C} = \mathrm{V}^{\mathrm{T}}\mathrm{DV}$, where $\mathrm{D_{jk}} = \lambda_{\mathbf{k}}\delta_{\mathrm{jk}}$ is a diagonal matrix of eigenvalues $\lambda_{\mathbf{k}}$, and the matrix V is an orthogonal matrix (hence $\mathrm{V}^{-1} = \mathrm{V}^{\mathrm{T}}$) whose columns are the eigenvectors $\hat{\mathbf{e}}_{\mathbf{k}}$.

In the coordinate system defined by $\hat{\mathbf{e}}_{\mathbf{k}}$, the off-diagonal elements are zero so the lateral dV_S/V_S structure is no longer correlated. In other words, each vector $\hat{\mathbf{e}}_{\mathbf{k}}$ defines a pattern of dV_S/V_S variations that is uncorrelated from that defined by any other linear combination of eigenvectors $\hat{\mathbf{e}}_{\mathbf{k'}\neq\mathbf{k}}$. The eigenvalues $\lambda_{\mathbf{k}}$ correspond to the variance of the pattern of lateral dV_S/V_S variations for the linear combination defined by $\hat{\mathbf{e}}_{\mathbf{k}}$. The eigenvector $\hat{\mathbf{e}}_{\mathbf{k}}$ that corresponds to the largest eigenvalue (in the absolute sense) is called the first principal component and determines the main mode of lateral variation in dV_S/V_S structure.

Figure 4 presents the lateral velocity patterns (maps) and corresponding eigenvectors $\hat{\mathbf{e}}_{\mathbf{k}}$ (depth profiles) of the first four principal components for S40RTS and S362ANI+M. As a sum, these four principal components account for more than 80% of the total variance in the models. We refer to them as the dominant patterns of dV_S/V_S variations in the mantle. For both models, the first principal component accounts for over half of the total variance in the models, and it corresponds to the tectonic pattern of velocity variations in the upper 250 km (i.e., the heterosphere). The second principal component in both models corresponds primarily to the signature of the large low-shear-velocity provinces (LLSVPs) at the base of the mantle and accounts for 14–17% of the total model variance. The third principal component, which accounts for 12–13% of total variance, mostly represents the accumulation of seismically fast slabs in the transition zone beneath the western Pacific and South America. It is only in the fourth principal component, which accounts for 5–6% of model variance, that significant differences between the tomographic models emerge. In S40RTS, the pattern of dV_S/V_S variations corresponding to this principal component traces the high-velocity Mesozoic slabs associated with Tethyan and Farallon subduction currently foundering in the mid-mantle. In S362ANI+M, this component highlights a nearly hemispheric pattern related to the relatively low dV_S/V_S found beneath the Pacific Basin in the upper mantle.

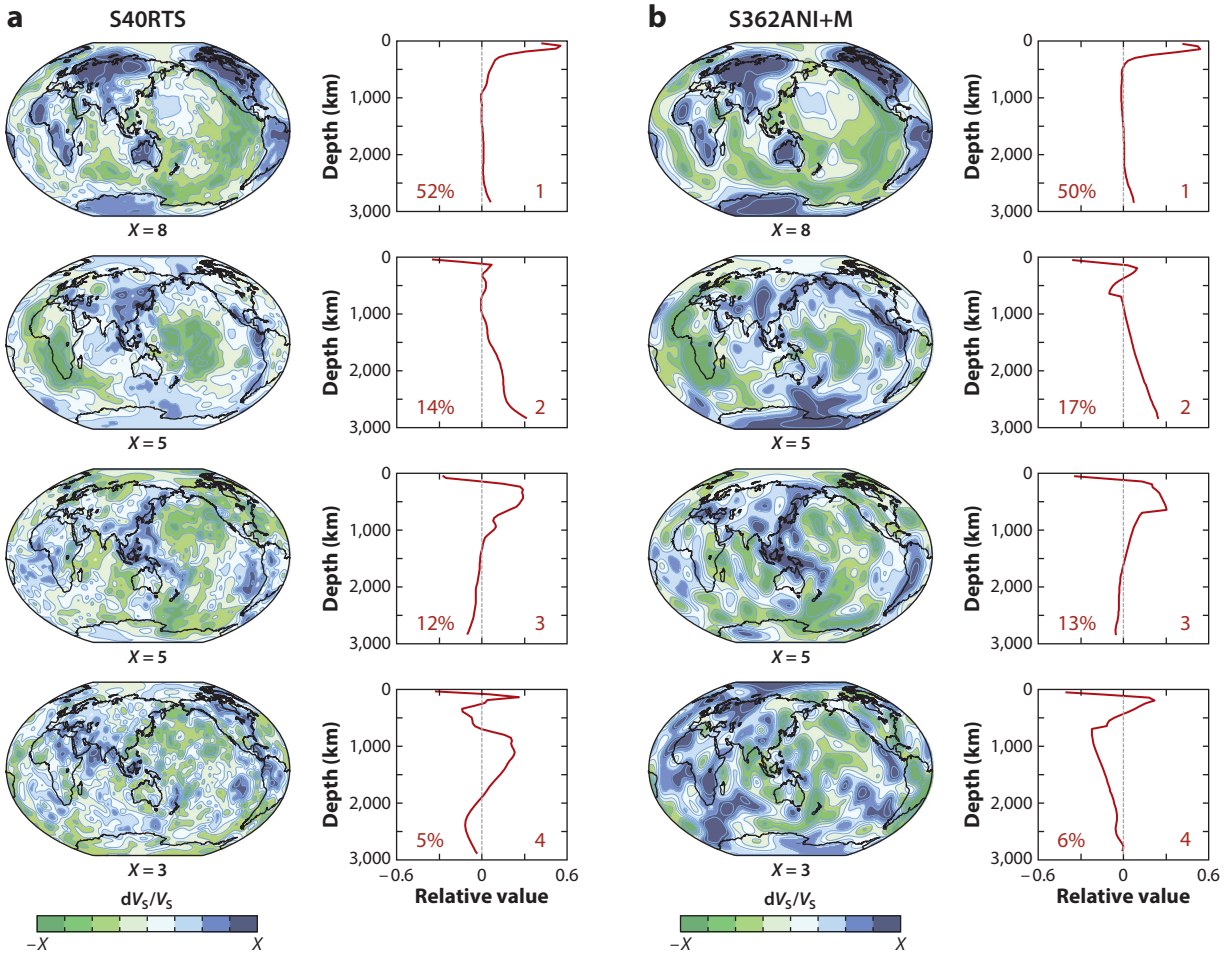

Figure 4

Principal component analysis of models (*a*) S40RTS (Ritsema et al. 2011) and (*b*) S362ANI+M (Moulik & Ekström 2014). The four components in order of the highest eigenvalues are shown from top to bottom. The eigenvalues are indicated in red text. The maps show dV_S/V_S structure with a range between $-X$ and $+X$ percent, indicated on the right.

Cluster Analysis

Lekić et al. (2012) applied *k*-means cluster analysis to classify shear-velocity profiles for the lower mantle from five tomographic models into two groups. These groups delineate geographically contiguous regions even though the classification is entirely based on similarity of the profiles and does not consider geographical position. One group corresponds to the LLSVPs and the other to the areas outside them. This allows intermodel consistency to be visualized by counting the number of models that classify the shear-velocity profile at that location to belong to the LLSVP group. Cottaar & Lekić (2016) extended this work to include a third group and used a moving depth window to assess intermodel consistency as a function of depth. **Figure 5** shows such depth-dependent vote maps for 14 tomographic models constructed using the implementation of Shephard et al. (2017) and visualized using SubMachine (Hosseini et al. 2018). The maps are displayed at 100-, 600-, 1,500-, and 2,800-km depth and illustrate the main features of tomographically imaged

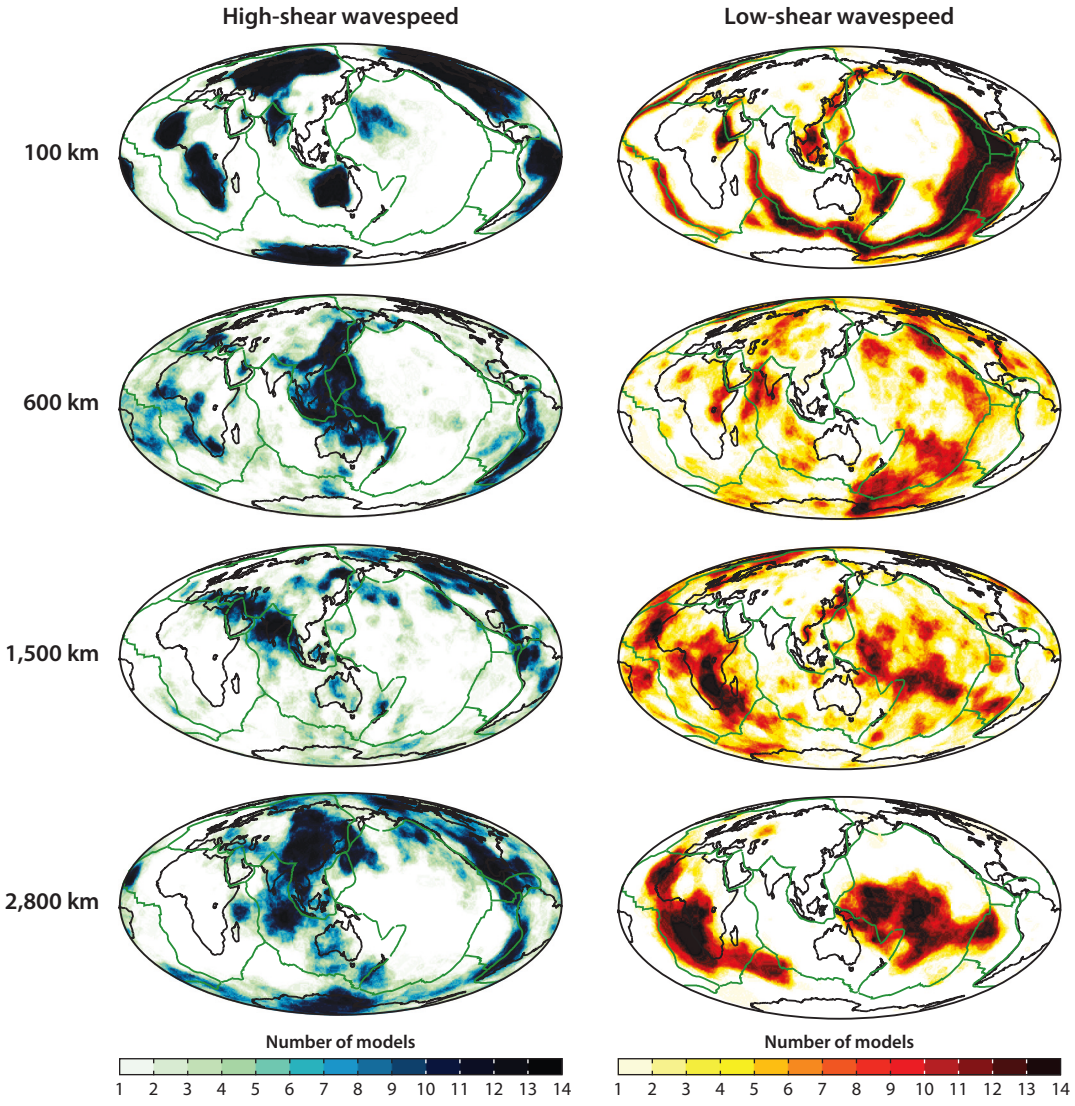

Figure 5

Vote maps for depths of (from *top* to *bottom*) 100, 600, 1,500, and 2,800 km. The models used are GyPSuM-S (Simmons et al. 2010), HMSL-S06 (Houser et al. 2008), PRI-S05 (Montelli et al. 2006), SP12RTS-S (Koelemeijer et al. 2016), S20RTS (Ritsema et al. 1999), S362ANI+M (Moulik & Ekström 2014), S40RTS (Ritsema et al. 2011), SAVANI (Auer et al. 2014), SAW642ANb (Panning et al. 2010), SEMUCB-WM1 (French & Romanowicz 2014), SEMum (Lekić & Romanowicz 2011), SGLOBE-rani (Chang et al. 2015), TX2015 (Lu & Grand 2016), and SEISGLOB2 (Durand et al. 2017). The columns on the left and right apply to high-velocity and low-velocity anomalies, respectively, with absolute shear-velocity perturbations larger than 1%.

velocity variations. At 100-km depth, the high-velocity structures correspond to the interiors of the continents that have not been modified by tectonic processes. The low-velocity structures outline the mid-ocean ridges, backarc basins, and tectonically active parts of eastern Africa and western North America. At 600-km depth, the high-velocity anomalies are subducted slabs in the MTZ beneath the circum-Pacific, Indonesia, South America, and Europe. The high-velocity structure that follows the Atlantic coastline of Africa may be related edge-driven convection

below the passive margin between the relatively thick lithosphere of western Africa and the much thinner oceanic lithosphere of the eastern Atlantic. This flow may cause intraplate volcanism in Africa (e.g., King & Ritsema 2000). Regions with anomalously low velocity are consistently seen beneath the East African Rift and western North America, where they are associated with continental extension; low velocities beneath the Indian Ocean and the southern Pacific have been more difficult to explain. At 1,500- and 2,800-km depth, the high-velocity structures are the remnants of the Tethys, Farallon, and Mongol-Okhotsk slabs of oceanic lithosphere that subducted into the mantle in the Permian period and the Mesozoic era. The low-velocity structures beneath Africa and the Pacific are the LLSVPs at the base of the mantle and low-velocity structure above them that rise more than 1,000 km above the CMB.

Spectrum of Heterogeneity

The mantle is heterogeneous on all scales, with tomographic models constraining large-scale variations and models of wave scattering constraining shorter scales. Typically, wave scattering models are stochastic in nature, describing the properties of the random medium. The relative ratio of large-scale to small-scale heterogeneity can be visualized by the power spectrum of velocity variations (dv/v). Global and continent-scale studies usually present the power spectrum as either power-per-spherical-harmonic-degree (e.g., Su & Dziewoński 1991) or power-per-octave (e.g., Meschede & Romanowicz 2015). The spectrum is defined as white and pink if the log of the power-per-degree and the power-per-octave, respectively, are constant with the log of the the spherical harmonic degree. When power-per-octave decreases with the log of the spherical harmonic degree, the spectrum is defined as red. Scattering-based studies, however, present the power spectrum as 1D (e.g., Mancinelli et al. 2016), 2D, or 3D (Sato et al. 2012) power-spectral density (PSD) as a function of wavenumber. The falloff of power with spherical harmonic degree and wavenumber depends crucially on these presentation choices (see Meschede & Romanowicz 2015 and Mancinelli et al. 2016 for discussion).

Figure 6 shows the constraints on the spectrum of mantle heterogeneity and its variation with depth from global, regional, and scattering-based studies, presented as (*a*) power-per-octave, (*b*) power-per-degree, and (*c*) 1D PSD. Slopes corresponding to white, pink, and red spectra of heterogeneity are also illustrated. We show the Voigt average dV_S/V_S variations from GLAD-M15 (Bozdağ et al. 2016), which is representative for all global V_S models. In the heterosphere, the spectrum is dominated by degree 5, reflecting the ocean-continent dichotomy. The spectrum of heterogeneity in the heterosphere captured by both global and regional models is red. The spectrum of heterogeneity in the transition zone is pink for both global and regional models. The spectra are also pink throughout the bulk of the lower mantle, albeit at lower power. Self-similar media are expected to have a pink spectrum of heterogeneity. Finally, in the CMB layer, the spectrum is red and dominated by degree 2, reflecting the two antipodal LLSVPs.

By modeling envelopes of 5–60-s period P-wave coda, Mancinelli et al. (2016) constrain heterogeneity in the upper mantle at shorter scales. They estimate a random medium defined by a von Karman autocorrelation function with a correlation length of 2,000 km, root-mean-square (RMS) perturbation of 10% ($\varepsilon = 0.1$), and exponent $\kappa = 0.05$. At small scales, this random medium is self-similar, possessing a pink spectrum of heterogeneity. Wave scattering studies indicate that small-scale heterogeneity persists in the lower mantle, albeit at an order of magnitude weaker RMS ($\varepsilon = 0.01$).

LARGE LOW-SHEAR-VELOCITY PROVINCES

In the lowermost mantle, regions with relatively low V_S form two broad, contiguous structures beneath the Pacific Ocean and beneath the Atlantic Ocean and southwestern Africa. These two

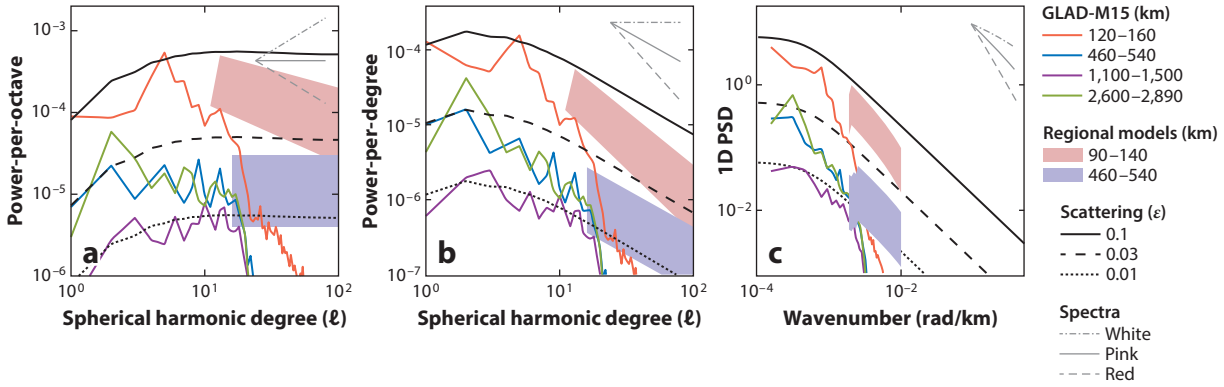

Figure 6

(*a*) Power-per-octave, (*b*) power-per-degree, and (*c*) 1D power-spectral density (PSD) of dv/v variations in a global model (GLAD-M15: Bozdağ et al. 2016), in the average of regional models, and from coda constraints on scattering. The solid black line represents the preferred model of Mancinelli et al. (2016), while dashed and dotted black lines represent von Karman media with identical correlation length and κ values but root-mean-square strength of heterogeneity of 0.03 and 0.01, respectively. For GLAD-M15, the red curve represents average structure in the 120–160-km depth range (i.e., the heterosphere); blue, 460–540 km (i.e., the mantle transition zone); purple, 1,100–1,500 km (i.e., the lower mantle); and green, 2,600–2,890 km (i.e., the core-mantle boundary layer). Regional averages are from Meschede & Romanowicz (2015) for the 90–140-km (*pink* field) and 460–540-km (*lavender* field) depth ranges. Solid, dashed, and dash-dotted gray lines denote slopes corresponding to pink, red, and white spectra of heterogeneity, respectively.

antipodal structures are conspicuous in all shear-velocity models of the lower mantle. Although originally called superplumes, they are commonly referred to as large low-shear-velocity provinces (LLSVPs) (e.g., Garnero et al. 2016), although V_P in them is also relatively low. The purely seismological acronym is intentional to avoid dynamical connotations.

Seismic Characteristics

V_S models agree on the areal extent of LLSVPs, as is evident from **Figure 5**. The geographic extent is primarily constrained by the travel times of diffracted S waves and ScS reflections off the core. While still substantial, agreement among models on the V_P structure is somewhat lesser, based on vote map evaluations (Cottaar & Lekić 2016, Hosseini et al. 2018), most likely because the sampling of the mantle by diffracted P waves and PcP waves is relatively poor. PcP is recorded only at epicentral distances shorter than about 60°, and diffracted P waves are typically much weaker than diffracted S waves, especially for long paths. Although recent efforts have improved the coverage of the deep mantle by direct and diffracted P waves (e.g., Euler & Wysession 2017), the effects of data coverage on the imaging must be carefully evaluated before interpreting the potential differences in V_P and V_S variations.

While LLSVPs are broad, the V_S structure above LLSVPs is complex and the radial extent of the low-velocity anomalies is more difficult to define. Above the African LLSVP, it appears to extend at least 1,000 km above the CMB with a northeasterly tilt (e.g., Ritsema et al. 1999). The connection between the LLSVPs in the lowermost mantle and low-velocity structures in the transition zone and upper mantle and with hotspot volcanism is suggested by more detailed regional tomographic studies (e.g., Civiero et al. 2015). The global distribution of hotspots weighted by flux has the same degree-2 pattern as V_S variations at the base of the mantle and low attenuation variations in the MTZ (Romanowicz & Gung 2002), suggesting that elevated temperatures associated with the LLSVPs persist throughout the lower mantle.

The density structure of mantle can be estimated from the splitting of normal modes. These long-period oscillations involve motions of large volumes of Earth material and are therefore affected by gravity and the density variations. The majority of seismic studies (Ishii & Tromp 1999, Trampert et al. 2004, Moulik & Ekström 2016) and studies of solid-Earth tides (Lau et al. 2017) indicate that the density in the LLSVPs is higher than their surroundings—a clarion signal of compositional heterogeneity. An exception is the study by Koelemeijer et al. (2017), who argued that relatively less dense LLSVPs better explain measurements of a unique set of Stoneley modes with focused sensitivity to structure at the CMB. Likely, the modeling results can be reconciled if only the lowermost (<100 km) part of the LLSVPs is anomalously dense, but future work should focus on incorporating full coupling in the measurement of mode splitting functions (Akbarashrafi et al. 2018), on assessing the depth range in which density and V_S variations might be anticorrelated, and on obtaining new constraints from CMB topography induced by mantle flow.

Studies of broadband data from regional networks have shown that shear waves traveling along the margins of LLSVPs are recorded with strongly variable delays for both S (Ritsema et al. 1998, Ni et al. 1999, Wen 2002) and P waves (e.g., Frost & Rost 2014) and with distorted or broadened waveforms (e.g., Ni et al. 2002, Sun et al. 2007, He & Wen 2009, Zhao et al. 2015). This indicates that V_S changes by several percent over less than 100-km distance across the margins of LLSVPs. Such strong gradients are often related to changes in rock composition because strong temperature gradients in the mantle cannot persist due to the high thermal diffusion. However, some geodynamical simulations suggest that flow in the mantle with a highly temperature-dependent rheology can result in variations in temperature that are sufficiently abrupt to sharp gradients in elastic properties (Davies et al. 2012).

Waveform modeling studies reveal 10–100-km-scale structures within or near the boundaries of the LLSVPs, including apparent gaps (He & Wen 2009, Kästle et al. 2017), variations beneath Hawaii (To et al. 2011), and high attenuation in the African LLSVP (Liu & Grand 2018). There are meso-scale structures with horizontal extents of several hundred kilometers including the Perm Anomaly (Lekić et al. 2012), a ridge-like structure beneath Kamchatka (He et al. 2014), and several anomalies that are currently at the limit of tomographic resolution (Cottaar & Lekić 2016). Observations of shear-wave splitting (e.g., Romanowicz & Wenk 2017) have been related to the alignment of former oceanic basaltic crust and pockets of partial melt and/or lattice-preferred orientation near the margins of LLSVPs. Thin layers (roughly 5- to 20-km thick) at the CMB with strong wavespeed reductions, called ultra-low velocity zones, are concentrated below and along the margins of the LLSVPs (see Yu & Garnero 2018 for a review).

The presence of compositional heterogeneity can also be assessed probabilistically, using tomographic inversions parameterized in terms of composition and temperature, which are related to V_P and V_S variations using thermodynamic relationships provided by mineral physics experiments, computations, and theory; this probabilistic tomography also supports large-scale compositional heterogeneity in the lowermost mantle (e.g., Trampert et al. 2004, Mosca et al. 2012). Additionally, models including compositional heterogeneity appear to fit the seismic heterogeneity spectrum in the lowermost mantle better than purely thermal models (e.g., McNamara 2019).

Geodynamic Interpretations

The competing models for the nature of LLSVPs can be divided into purely thermal or thermochemical models. (See McNamara 2019 for a review.) In purely thermal models, LLSVPs are regarded as tightly clustered upwellings that are imaged tomographically as broad structures due to the intrinsically low resolution of seismic models (e.g., Davies et al. 2012, McNamara 2019). Convection in these models is driven entirely by thermal buoyancy. Sinking of relatively dense

subducted slabs produces a downwelling flow regime around the Pacific and African lower mantle. Upwellings, including mantle plumes, appear to form preferentially in the LLSVPs far from current and paleo-subduction zones, potentially resulting in excessive (hotspot) volcanism and anomalous (dynamic) topography (see Flament et al. 2013).

In thermochemical models, compositional buoyancy contributes to convection. The compositional distinct material could be primordial in nature, produced after early planetary differentiation: leftover dense silicate (Labrosse et al. 2007, Lee et al. 2010) or metallic melts (Zhang et al. 2016) or crust formed on the early Earth or both. Alternatively, LLSVPs may have formed over Earth's history by the steady accumulation of subducted oceanic crust that segregated from the slabs and sank to the bottom of the mantle (see Tackley 2012 for a review). Hybrid models in which the lowermost portions of the LLSVPs are primordial and overlying regions enriched in basalt have also been proposed (Ballmer et al. 2016). LLSVPs may be continually modified by incorporation of subducted material (e.g., Li et al. 2014), chemical reactions with the surrounding mantle, and underlying core, as well as potentially from volatile elements transported into the deep Earth by subducted plates. Upwelling mantle plumes may originate from the thermochemical piles and produce distinct trace-element signatures observed in hotspot lavas (Garnero et al. 2016).

If their densities are relatively high, LLSVPs may be stable for a long geologic time and be deformed and displaced by convective flow in the mantle. Indeed, plate motion–driven geodynamical models in which LLSVPs are inherently dense thermochemical structures can explain the current position and general shape of LLSVPs (McNamara & Zhong 2005). Dziewoński et al. (2010) proposed that they exert control on the planform of convection, perhaps by stabilizing the locations of upwellings.

MANTLE PLUMES

Mantle plumes begin as instabilities in a thermal boundary layer, whether in the immediate vicinity of the CMB or at the margins of inherently dense and hot LLSVPs (Davaille 1999, Jellinek & Manga 2002). As they rise, plumes may carry compositional heterogeneity from the LLSVPs and surrounding regions to the surface (e.g., Farnetani & Hofmann 2009) and produce hotspot volcanism with distinct geochemical characteristics (e.g., White 2015). Compositional heterogeneity in plumes may cause plumes to rise only when they become sufficiently broad for thermal buoyancy to compensate for the intrinsic high density.

Burke & Torsvik (2004) hypothesized that plumes responsible for the large igneous provinces (LIPs) formed primarily along the margins of the LLSVPs; the correlation between restored locations of LIPs and present-day LLSVP margins implied that the latter have maintained their configurations since the Permian. However, whether there is a correlation between the LIP locations and the margins of LLSVPs and whether LLSVPs can remain fixed for hundreds of millions of years in the mantle remain debated (see McNamara 2019).

Tomographic imaging results and interpretations of focused upwelling flow (i.e., mantle plumes) are often controversial. Although global seismic images contain elongated low-velocity structures suggestive of plumes, it is rare that the same seismic structures are reproduced independently. **Figure 7** illustrates this for vertical cross sections through four hotspots in the Pacific according to 11 V_S models. Although the large-scale V_S structure is similar, the strength, shape, and vertical extent of the low-velocity anomalies beneath the hotspots vary because the images are based on different data sets and modeling approaches. Understanding the image differences requires an evaluation of image resolution (e.g., Styles et al. 2011) and analyses of how plumes distort waveforms.

Narrow, purely thermal plumes do not distort passing seismic waves strongly, which renders them virtually invisible to traditional tomographic techniques. Due to an effect called wavefront

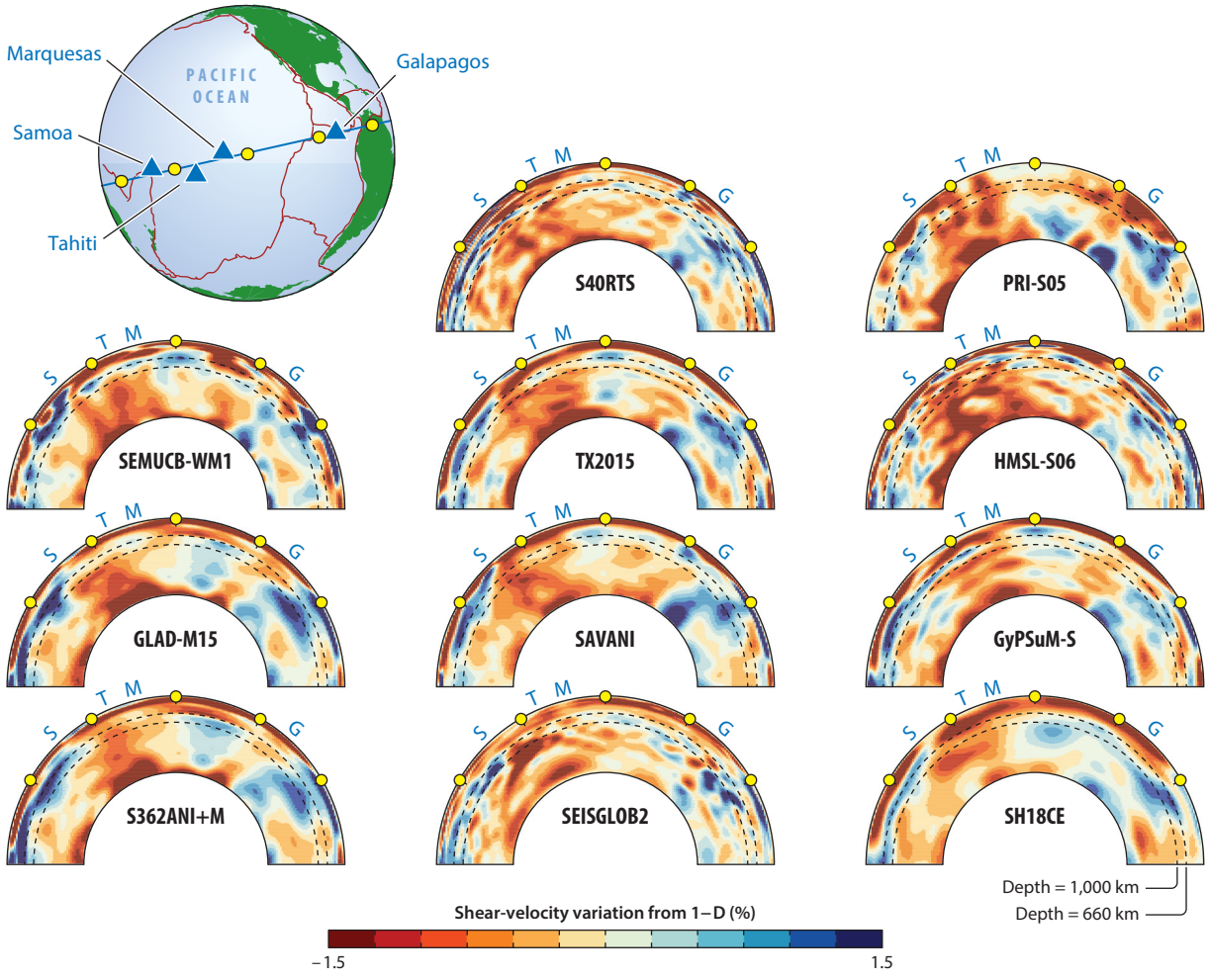

Figure 7

Cross sections through 11 S-wave models of the mantle along a transect through the Pacific, including the (from west to east) Samoa (S), Tahiti (T), Marquesas (M), and Galapagos (G) hotspots. The seismic models are SEMUCB-WM1 (French & Romanowicz 2014), GLAD-M15 (Bozdağ et al. 2016), S362ANI+M (Moulik & Ekström 2014), S40RTS (Ritsema et al. 2011), TX2015 (Lu & Grand 2016), SAVANI (Auer et al. 2014), SEISGLOB2 (Durand et al. 2017), PRI-S05 (Montelli et al. 2006), HMSL-S06 (Houser et al. 2008), GyPSuM-S (Simmons et al. 2010), and SH18CE (Takeuchi 2007). To simplify the plotting, the images have been reparameterized using the S40RTS parameterization, resulting in minor smoothing.

healing (e.g., Gudmundsson 1996), seismic waves that have interacted with a plume in the lower mantle restore their original wavefront during propagation to seismic stations on the surface. Using computations of 3D waveforms, Hwang et al. (2011) and Maguire et al. (2016) showed that the expected shifts (i.e., delays) of long-period body waves due to thermal plumes in the lower mantle are less than a second. Ray-theoretical and full waveform inversions of teleseismic travel times indicate that the signal from purely thermal plumes with relatively narrow tails in the lower mantle may be invisible to tomographic imaging methods for realistic source-receiver geometries (Maguire et al. 2018). Rickers et al. (2012) demonstrated that the modeling of the coda of P waves and S waves that include diffracted waves around plumes could improve tomographic resolution

of narrow plume conduits. However, these diffractions are weak and may only be detectable by applying array techniques to waveform data, ideally from dense seismic networks (e.g., Ji & Nataf 1998, Stockmann et al. 2019).

If intraoceanic plumes are present beneath hotspots such as Iceland, Kerguelen, Hawaii, Samoa, and Pitcairn and broader than about 500 km, they could be tomographically resolvable. Although tomographic evidence for the presence of plume-like low-velocity anomalies in the deep mantle has been presented for Iceland (e.g., Bijwaard et al. 1998), Hawaii (Wolfe et al. 2009), and other hotspots around the world (e.g., Zhao 2004), the study by Montelli et al. (2004) was the first to claim detections of more than 20 plumes, estimating them to be wider than 500 km. Although the study was controversial at the time (see, e.g., de Hoop & van der Hilst 2005), later independent studies resolved whole-mantle plume-like seismic structures.

The study by French & Romanowicz (2015) is based on full waveform inversions including portions of the waveform that may contain wave diffractions due to small-scale structure in the deep mantle such as plumes. The authors interpret their images of 11 plumes as being even broader and stronger than those cataloged by Montelli et al. (2004), which may imply that they contain compositionally distinct materials with relatively high density because the plume must develop a large volume to become buoyant. The low-velocity anomalies below the Pacific appear to be rooted in or near the Pacific LLSVP and are distinct and continuous vertical structures between the CMB and about 1,000-km depth, without substantial deflection by background mantle flow. At depths shallower than 1,000 km, the low-velocity anomalies appear to deflect (e.g., Rickers et al. 2013, French & Romanowicz 2015, Rudolph et al. 2015) and may merge with subasthenospheric low-velocity structures in the upper mantle (French et al. 2013).

MANTLE DOWNWELLING REGIONS

Higher-than-average shear and compressional wavespeeds in the mantle are observed beneath current and past subduction zones. Seismic tomography therefore tells us how the MTZ affects the subduction of relatively cool oceanic lithosphere, and it can be used to unravel plate motions and plate boundary configurations in the geologic past. Early P-wave models from the late 1980s and early 1990s focused on the structure of slabs in the mantle beneath the western Pacific and Europe (e.g., Lay 1994). These studies provided the first evidence that some slabs appear to lay flat above the 660 km (e.g., Izu-Bonin, Honshu) while others have crossed the 660 km (e.g., Marianas, Aegean). In the mantle down to about 1,500-km depth, two prominent elongated anomalies beneath North and South America and beneath Eurasia have been associated with the subduction of the Farallon Plate beneath North America and oceanic plate subduction related to the closure of the Tethys Sea beneath Eurasia in the Jurassic. Subsequent travel-time models have refined images of the P-wave (e.g., Obayashi et al. 2013) and the S-wave structure (e.g., Lu & Grand 2016) in subduction zones around the world.

Fukao et al. (2001) categorize the descent of slabs into two groups. The so-called stagnant slabs in the first group are connected to plates presently subducting. Slabs in the second group are related to ancient subduction zones. They are presently sinking in the lower mantle, although the shallowest segments that subducted most recently may still be present in the MTZ. Fukao & Obayashi (2013) argued for a third group of slabs (e.g., Java, Kermadec, and Peru) that appear stagnant above about 1,000-km depth, suggesting that the uppermost lower mantle can also be a reservoir, albeit temporary, of subducting slabs. The stagnation of slabs in the uppermost lower mantle has been attributed to enhanced slab buoyancy due to either the delayed diffusion of pyroxene into garnet (King et al. 2015) or enrichment of the ambient mantle with relatively dense basaltic components (Ballmer et al. 2015), as predicted by simulations of mantle circulation (e.g.,

Nakagawa & Tackley 2004). Alternatively, a viscosity increase at around 1,000-km depth can result in slab stagnation and plume deflection at this depth (Rudolph et al. 2015); the origin of this increase remains uncertain.

Slab Stagnation in the Mantle Transition Zone

Slab warping and stagnation in the MTZ is a consequence of the resistance of the lower mantle to downward flow. The resistance is due to a combination of the endothermic nature of the 660-km phase transition and the increase in viscosity by an order or two orders of magnitude. First, the 660-km phase transition, involving a density increase of about 220 kg/m^3, occurs deeper in a relatively cool slab. The deflection of the phase boundary by tens of kilometers, depending on the steepness of the Clapeyron slope of the ringwoodite-to-postspinel transition, estimated to be −0.4 to −2.0 MPa/K (Katsura et al. 2003, Fei et al. 2004), provides local buoyancy. Second, the increase of viscosity by one to two orders of magnitude reduces the sinking rate of slabs to about 1 cm/year in the lower mantle (e.g., van der Meer et al. 2018). Goes et al. (2017) determined from reviewing observational constraints and geodynamic modeling results that trench retreat is an additional factor in slab flattening and stagnation in the MTZ, especially in older subduction zones where subducting plates are cooler and therefore stronger.

Slab flattening is also evident from analyses of the depths of the 410- and 660-km phase transitions and especially the thickness of the mantle between the 410 and the 660 km, sometimes referred to as the thickness of the MTZ. Cooling of the MTZ by subducted lithosphere results in the thickening of the MTZ because the Clayeron slopes of the olivine-to-wadsleyite (at the 410 km) and ringwoodite-to-postspinel phases (at the 660 km) have opposite signs. Global studies of shear wave reflections (i.e., *SS* precursors) at discontinuities in the MTZ (e.g., Flanagan & Shearer 1998) indicate that the MTZ is thickest beneath the western Pacific. The relatively large difference between the arrival times of *SS* reflections at the 410- and 660-km phase transitions indicates that, over a relatively wide region, these boundaries are separated by several tens of kilometers, more than elsewhere in the mantle. From a receiver function analysis of recordings from the Hi-net array in Japan, Niu et al. (2005) inferred that the downward deflection of the 660-km phase transition beneath southwest Japan is much wider than the upwarping of the 410-km updip along the slab. This is consistent with the relatively steep descent of the Pacific slab through the 410 km and its flattening above the 660 km.

Slab Descent in the Lower Mantle

Dynamic modeling indicates that flat slabs in the MTZ will eventually fold, thicken, and sink into the lower mantle when they are at least two orders of magnitude more viscous than the surrounding mantle (see Goes et al. 2017 for a review). By identifying high-velocity anomalies in tomographic images as fragments of subducted slabs, researchers have used seismic tomography to constrain paleo-subduction, paleogeography, and the tectonic history of plate motions (e.g., van der Voo et al. 1999, Sigloch & Mihalynuk 2013, van der Meer et al. 2018). We note that fast anomalies related to sinking slabs appear less radially continuous than slow anomalies in the lower mantle (Dziewoński et al. 2010).

The earliest work focused on the so-called Farallon, Tethys, and Mongol-Okhotsk anomalies, which were recognized first in travel-time models of both P-wave and S-wave velocity (e.g., Grand et al. 1997) and are the prominent and most consistent anomalies in seismic tomography (see **Figure 4**). **Figure 8** compares maps of P-wave velocities to reconstructed tectonic settings from 120 and 240 million years ago to associate ancient subduction zones with high-velocity and presumably cool regions of the deep mantle. Using these three well-studied slab structures as anchor

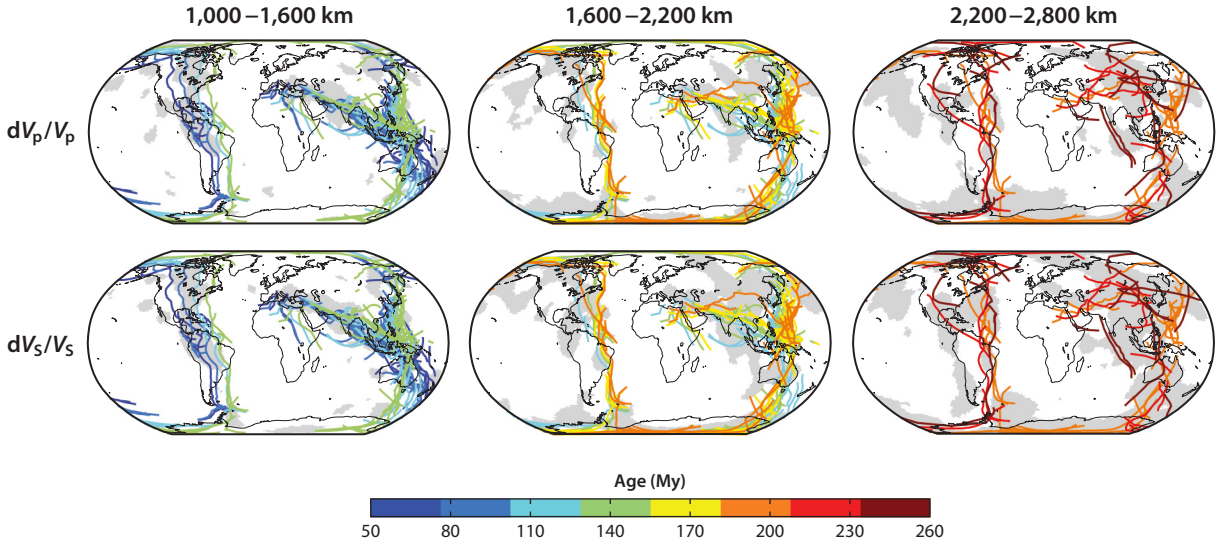

Figure 8

Relationship between restored locations of Mesozoic subduction zones and higher-than-average V_P (*top*) and V_S (*bottom*) tomographic models. Subduction zone locations are from the model of Young et al. (2019) and are colored by age from 50 My (*dark blue*) to 260 My (*dark red*). In gray-shaded regions, a majority of the S-wave or P-wave tomographic models classify the wavespeed averaged over 1,300–1,800- (*left*), 1,600–2,200- (*middle*), and 2,000–2,500-km (*right*) depth as belonging to the faster-than-average cluster, following Cottaar & Lekić (2016).

slabs, van der Meer et al. (2018) related 96 additional albeit smaller anomalies in P-wave model UU-P07 and S-wave model S40RTS to geologic evidence for accretion and mountain building from as early as 300 million years ago. The study assumes that slabs sink vertically and that the ages of the top and bottom of the high-velocity anomalies are correlated with the onset and termination of orogenesis. However, Domeier et al. (2016) argue that resolved anomalies in S-wave tomography to a depth of 2,300 km correlate with reconstructed subduction zones of only the last 130 Myr.

Additional support for the presence of slab fragments in the lower mantle comes from studies of high-frequency scattering. In particular, the conversion of S waves to P waves by fragments of subducted oceanic crust in the lower mantle to a depth of 1,700 km has been located below subduction zones in numerous seismic networks around the world by array processing techniques (see Kaneshima 2019 for a recent review).

OUTLOOK

In addition to mapping V_P and V_S separately, we highlight four aspects of global tomography that deserve continuing efforts. First, new joint analysis of V_P and V_S is key to understanding the nature of heterogeneity, such as the effects of spin transition in the mid-mantle (Lin et al. 2013) and the distribution of postperovskite in the lowermost mantle (e.g., Shim 2008). Because it is less sensitive to both attenuation and the presence of postperovskite, V_P is a better proxy for temperature than is V_S, particularly at the base of the mantle, where it can be used to estimate heat flux variations across the CMB (e.g., Hernlund & McNamara 2015). Second, the mapping of the 3D attenuation structure of the lower mantle, still in its infancy, will add constraints on the thermal structure of the mantle as well as on the pathways of water, carbon, and melts (Stixrude & Jeanloz 2015). Third, constraints on anisotropy inform us of the deformation of mantle materials

due to the interactions of, for example, subducted slabs with the CMB and upward flow along and above LLSVPs (e.g., Romanowicz & Wenk 2017). Finally, we argue that Earth's density structure, perhaps the most essential parameter for understanding the nature of LLSVPs, is still poorly constrained. The uncertainties arise from modeling assumptions including regularization, parameterization, and approximations in accounting for mode coupling and observational uncertainty due to noise. Akbarashrafi et al. (2018) demonstrate that commonly made mode coupling approximations produce errors of magnitude similar to the signal expected from density variations. However, the mode that most strongly prefers dense LLSVPs is the longest-period mode of Earth, ${}_0S_2$ (Moulik & Ekström 2016), for which commonly made coupling approximations have less effect (Akbarashrafi et al. 2018). Resovsky & Ritzwoller (1999) and Kuo & Romanowicz (2002) discuss modeling trade-offs between velocity and density structures.

Seismology will advance by improvements in station coverage, particularly in the oceans, and by the growth in computer power that will enable seismologists to accurately simulate wave propagation at higher frequencies and to model V_P and V_S structures at increasingly small scales. It is likely that machine learning will foster many advancements in mining the millions of archived seismograms and accelerate forward simulations for model space search approaches (e.g., Bergen et al. 2019). Seismic signals of core and deep-mantle phases can be extracted using seismic interferometry (e.g., Poli et al. 2012, Spica et al. 2017, Phạm et al. 2018), expanding data coverage. New seismograms from ocean-bottom (Suetsugu & Shiobara 2014) and floating seismometers (Nolet et al. 2019) have the potential for much-improved imaging of the mantle beneath oceans, particularly for V_P. Transformative technologies such as distributed acoustic sensing using submarine fiber-optic cables offer the promise of unprecedented density of seismic recordings across ocean basins (Marra et al. 2018). Seismology on Mars (Lognonné et al. 2019), the Moon (Weber et al. 2018), and icy satellites (Vance et al. 2018) opens the door for comparative planetology.

DISCLOSURE STATEMENT

The authors are not aware of any affiliations, memberships, funding, or financial holdings that might be perceived as affecting the objectivity of this review.

ACKNOWLEDGMENTS

Application of PCA to tomographic models originated through collaboration with Barbara Romanowicz and Adam Dziewoński. We thank Paula Koelemeijer for help with calculating point spread functions. We acknowledge financial support from the Packard Foundation and NSF grant CAREER EAR-1352214 to V.L. and NSF grants EAR-1644829 and EAR-1565511 to J.R.

LITERATURE CITED

Akbarashrafi F, Al-Attar D, Deuss A, Trampert J, Valentine AP. 2018. Exact free-oscillation spectra, splitting functions and the resolvability of Earth's density structure. *Geophys. J. Int.* 213(1):58–76

Auer L, Boschi L, Becker TW, Nissen-Meyer T, Giardini D. 2014. *Savani*: a variable resolution whole-mantle model of anisotropic shear velocity variations based on multiple data sets. *J. Geophys. Res. Solid Earth* 119:3006–34

Ballmer MD, Schmerr NC, Nakagawa T, Ritsema J. 2015. Compositional mantle layering revealed by slab stagnation at ~1000-km depth. *Sci. Adv.* 1(11):e1500815

Ballmer MD, Schumacher L, Lekić V, Thomas C, Ito G. 2016. Compositional layering within the large low shear-wave velocity provinces in the lower mantle. *Geochem. Geophys. Geosyst.* 17:5056–77

Bergen KJ, Johnson PA, de Hoop MV, Beroza GC. 2019. Machine learning for data-driven discovery in solid Earth geoscience. *Science* 363(6433):eaau0323

Bijwaard H, Spakman W, Engdahl ER. 1998. Closing the gap between regional and global tomography. *J. Geophys. Res.* 103:30005–78

Bozdağ E, Peter D, Lefebvre M, Komatitsch D, Tromp J, et al. 2016. Global adjoint tomography: first-generation model. *Geophys. J. Int.* 207(3):1739–66

Burdick S, Lekić V. 2017. Velocity variations and uncertainty from transdimensional *P*-wave tomography of North America. *Geophys. J. Int.* 209:1337–51

Burke K, Torsvik TH. 2004. Derivation of large igneous provinces of the past 200 million years from long-term heterogeneities in the deep mantle. *Earth Planet. Sci. Lett.* 227(3–4):531–38

Chang S-J, Ferreira AMG. 2017. Improving global radial anisotropy tomography: the importance of simultaneously inverting for crustal and mantle structure. *Bull. Seismol. Soc. Am.* 107(2):624–38

Chang S-J, Ferreira AMG, Ritsema J, van Heijst HJ, Woodhouse JH. 2015. Joint inversion for global isotropic and radially anisotropic mantle structure including crustal thickness perturbations. *J. Geophys. Res. Solid Earth* 120:4278–300

Civiero C, Hammond JOS, Goes S, Fishwick S, Ahmed A, et al. 2015. Multiple mantle upwellings in the transition zone beneath the northern East-African Rift system from relative P-wave travel-time tomography. *Geochem. Geophys. Geosyst.* 16:2949–68

Cottaar S, Lekić V. 2016. Morphology of seismically slow lower-mantle structures. *Geophys. J. Int.* 207(2):1122–36

Dahlen FA, Hung S-H, Nolet G. 2000. Fréchet kernels for finite-frequency traveltimes—I. Theory. *Geophys. J. Int.* 141:157–74

Davaille A. 1999. Simultaneous generation of hotspots and superswells by convection in a heterogenous planetary mantle. *Nature* 402:756–60

Davies DR, Goes S, Davies JH, Schuberth BSA, Bunge HP, Ritsema J. 2012. Reconciling dynamic and seismic models of Earth's lower mantle: the dominant role of thermal heterogeneity. *Earth Planet. Sci. Lett.* 353–354:253–69

de Hoop M, van der Hilst R. 2005. On sensitivity kernels for 'wave equation' transmission tomography. *Geophys. J. Int.* 160:621–33

de Wit RWL, Käufl PJ, Valentine AP, Trampert J. 2014. Bayesian inversion of free oscillations for Earth's radial (an)elastic structure. *Phys. Earth Planet. Inter.* 237:1–17

Debayle E, Ricard Y. 2012. A global shear velocity model of the upper mantle from fundamental and higher Rayleigh mode measurements. *J. Geophys. Res.* 117(B10):B10308

Domeier MP, Doubrovine V, Torsvik TH, Spakman W, Bull AL. 2016. Global correlation of lower mantle structure and past subduction. *Geophys. Res. Lett.* 43:4945–53

Durand S, Debayle E, Ricard Y, Zaroli C, Lambotte S. 2017. Confirmation of a change in the global shear velocity pattern at around 1000 km depth. *Geophys. J. Int.* 211(3):1628–39

Dziewoński AM, Anderson DL. 1981. Preliminary reference earth model. *Phys. Earth Planet. Inter.* 25:297–356

Dziewoński AM, Hager BH, O'Connell RJ. 1977. Large-scale heterogeneities in the lower mantle. *J. Geophys. Res.* 82(2):239–55

Dziewoński AM, Lekić V, Romanowicz BA. 2010. Mantle anchor structure: an argument for bottom up tectonics. *Earth Planet. Sci. Lett.* 299:69–79

Euler GG, Wysession ME. 2017. Geographic variations in lowermost mantle structure from the ray parameters and decay constants of core-diffracted waves. *J. Geophys. Res. Solid Earth* 122(7):5369–94

Farnetani CG, Hofmann AW. 2009. Dynamics and internal structure of a lower mantle plume conduit. *Earth Planet. Sci. Lett.* 282(1–4):314–22

Fei Y, Van Orman J, Li J, Van Westrenen W, Sanloup C, et al. 2004. Experimentally determined postspinel transformation boundary in Mg_2SiO_4 using MgO as an internal pressure standard and its geophysical implications. *J. Geophys. Res.* 109(B2):B02305

Fichtner A, Kennett BLN, Igel H, Bunge H-P. 2009. Full seismic waveform tomography for upper-mantle structure in the Australasian region using adjoint methods. *Geophys. J. Int.* 179:1703–25

Fichtner A, Trampert J. 2011. Resolution analysis in full waveform inversion. *Geophys. J. Int.* 187:1604–24

Fichtner A, van Leeuwen T. 2015. Resolution analysis by random probing. *J. Geophys. Res. Solid Earth* 120:5549–73

Flament N, Gurnis M, Müller RD. 2013. A review of observations and models of dynamic topography. *Lithosphere* 5(2):189–210
Flanagan MP, Shearer PM. 1998. Global mapping of topography on transition zone velocity discontinuities by stacking of *SS* precursors. *J. Geophys. Res.* 103(B2):2673–92
French S, Lekić V, Romanowicz B. 2013. Waveform tomography reveals channeled flow at the base of the oceanic asthenosphere. *Science* 342(6155):227–30
French SW, Romanowicz B. 2015. Broad plumes rooted at the base of the Earth's mantle beneath major hotspots. *Nature* 525:95–99
French SW, Romanowicz BA. 2014. Whole-mantle radially anisotropic shear velocity structure from spectral-element waveform tomography. *Geophys. J. Int.* 199(3):1303–27
Frost DA, Rost S. 2014. The P-wave boundary of the Large-Low Shear Velocity Province beneath the Pacific. *Sci. Lett.* 403:380–92
Fukao Y, Obayashi M. 2013. Subducted slabs stagnant above, penetrating through, and trapped below the 660 km discontinuity. *J. Geophys. Res. Solid Earth* 118:5920–38
Fukao Y, Widiyantoro S, Obayashi M. 2001. Stagnant slabs in the upper and lower mantle transition region. *Rev. Geophys.* 39(3):291–323
Gao C, Lekić V. 2018. Consequences of parametrization choices in surface wave inversion: insights from transdimensional Bayesian methods. *Geophys. J. Int.* 215(2):1037–63
Garnero EJ, McNamara AK, Shim S-H. 2016. Continent-sized anomalous zones with low seismic velocity at the base of Earth's mantle. *Nat. Geosci.* 9:481–89
Goes S, Agrusta R, van Hunen J, Garel F. 2017. Subduction-transition zone interaction: a review. *Geosphere* 13(3):644–64
Grand SP, van der Hilst RD, Widiyantoro S. 1997. High resolution global tomography: a snapshot of convection in the Earth. *GSA Today* 7:1–7
Gudmundsson O. 1996. On the effect of diffraction on traveltime measurements. *Geophys. J. Int.* 124(1):304–14
He Y, Wen L. 2009. Structural features and shear-velocity structure of the "Pacific Anomaly." *J. Geophys. Res.* 114(B2):B02309
He Y, Wen L, Zheng T. 2014. Seismic evidence for an 850 km thick low-velocity structure in the Earth's lowermost mantle beneath Kamchatka. *Geophys. Res. Lett.* 41:7073–79
Hernlund JW, McNamara AK. 2015. The core-mantle boundary region. In *Treatise on Geophysics*, ed. G Schubert, pp. 461–519. Oxford, UK: Elsevier. 2nd ed.
Ho T, Priestley K, Debayle E. 2016. A global horizontal shear velocity model of the upper mantle from multimode Love wave measurements. *Geophys. J. Int.* 207(1):542–61
Hosseini K, Matthews KJ, Sigloch K, Shephard GE, Domeier M, Tsekhmistrenko M. 2018. SubMachine: web-based tools for exploring seismic tomography and other models of Earth's deep interior. *Geochem. Geophys. Geosyst.* 19:1464–83
Houser C, Masters G, Shearer P, Laske G. 2008. Shear and compressional velocity models of the mantle from cluster analysis of long-period waveforms. *Geophys. J. Int.* 174:195–212
Hwang YK, Ritsema J, van Keken PE, Goes S, Styles E. 2011. Wavefront healing renders deep plumes seismically invisible. *Geophys. J. Int.* 187:273–77
IRIS DMC. 2014. *Global stacks of millions of seismograms*. Data Services Products: Globalstacks. **https://doi.org/10.17611/DP/GS.1**
Irving JC, Cottaar S, Lekić V. 2018. Seismically determined elastic parameters for Earth's outer core. *Sci. Adv.* 4:eaar2538
Ishii M, Tromp J. 1999. Normal-mode and free air gravity constraints on lateral variations in velocity and density of Earth's mantle. *Science* 285(5431):1231–36
Jellinek AM, Manga M. 2002. The influence of a chemical boundary layer on the fixity, spacing and lifetime of mantle plumes. *Nature* 418:760–63
Ji Y, Nataf H. 1998. Detection of mantle plumes in the lower mantle by diffraction tomography: Hawaii. *Earth Planet. Sci. Lett.* 159:99–115
Kaneshima S. 2018. Array analyses of SmKS waves and the stratification of Earth's outermost core. *Phys. Earth Planet. Inter.* 276:234–46

Kaneshima S. 2019. Seismic scatterers in the lower mantle near subduction zones. *Geophys. J. Int.* 218(3):1873–91

Kästle ED, Weber M, Krüger F. 2017. Complex deep structure of the African low-velocity zone. *Bull. Seismol. Soc. Am.* 107(4):1688–703

Katsura T, Yamada H, Shinmei T, Kubo A, Ono S, et al. 2003. Post-spinel transition in Mg_2SiO_4 determined by high *P–T* in situ X-ray diffractometry. *Phys. Earth Planet. Inter.* 136:11–24

King SD, Frost DJ, Rubie DC. 2015. Why cold slabs stagnate in the transition zone. *Geology* 43:231–34

King SD, Ritsema J. 2000. African hotspot volcanism: small-scale convection in the upper mantle beneath cratons. *Science* 290:1137–40

Koelemeijer P, Deuss A, Ritsema J. 2017. Density structure of Earth's lowermost mantle from Stoneley mode splitting observations. *Nat. Commun.* 8:15241

Koelemeijer P, Ritsema J, Deus A, van Heijst HJ. 2016. SP12RTS: a degree-12 model of shear- and compressional-wave velocity for Earth's mantle. *Geophys. J. Int.* 204(2):1024–39

Komatitsch D, Tromp J. 2002. Spectral-element simulations of global seismic wave propagation—I. Validation. *Geophys. J. Int.* 149(2):390–412

Krischer L, Fichtner A, Boehm C, Igel H. 2018. Automated large-scale full seismic waveform inversion for North America and the North Atlantic. *J. Geophys. Res. Solid Earth* 123:5902–28

Kuo C, Romanowicz B. 2002. On the resolution of density anomalies in the Earth's mantle using spectral fitting of normal-mode data. *Geophys. J. Int.* 150:162–79

Kustowski B, Ekström G, Dziewoński AM. 2008. Anisotropic shear-wave velocity structure of the Earth's mantle: a global model. *J. Geophys. Res.* 113(B6):B06306

Labrosse S, Hernlund JW, Coltice N. 2007. A crystallizing dense magma ocean at the base of the Earth's mantle. *Nature* 450:866–69

Lau HC, Mitrovica JX, Davis JL, Tromp J, Yang HY, Al-Attar D. 2017. Tidal tomography constrains Earth's deep-mantle buoyancy. *Nature* 551(7680):321–26

Lay T. 1994. The fate of descending slabs. *Annu. Rev. Earth Planet. Sci.* 22:33–61

Lee C-TA, Luffi P, Höink T, Li J, Dasgupta R, Hernlund J. 2010. Upside-down differentiation and generation of a 'primordial' lower mantle. *Nature* 463:930–33

Lekić V, Cottaar S, Dziewoński A, Romanowicz B. 2012. Cluster analysis of global lower mantle tomography: a new class of structure and implications for chemical heterogeneity. *Earth Planet. Sci. Lett.* 357:68–77

Lekić V, Romanowicz B. 2011. Inferring upper-mantle structure by full waveform tomography with the spectral element method. *Geophys. J. Int.* 185(2):799–831

Leng K, Nissen-Meyer T, van Driel M, Hosseini K, Al-Attar D. 2019. AxiSEM3D: broad-band seismic wavefields in 3-D global earth models with undulating discontinuities. *Geophys. J. Int.* 217(3):2125–46

Li C, van der Hilst RD, Engdahl ER, Burdick S. 2008. A new global model for *P* wave speed variations in Earth's mantle. *Geochem. Geophys. Geosyst.* 9(5):Q05018

Li M, McNamara AK, Garnero EJ. 2014. Chemical complexity of hotspots caused by cycling oceanic crust through mantle reservoirs. *Nat. Geosci.* 7(5):366–70

Li XD, Romanowicz B. 1995. Comparison of global waveform inversions with and without considering cross branch coupling. *Geophys. J. Int.* 121:695–709

Li XD, Romanowicz B. 1996. Global mantle shear velocity model developed using nonlinear asymptotic coupling theory. *J. Geophys. Res.* 101(B10):22245–72

Lin JF, Speziale S, Mao Z, Marquardt H. 2013. Effects of the electronic spin transitions of iron in lower mantle minerals: implications for deep mantle geophysics and geochemistry. *Rev. Geophys.* 51(2):244–75

Liu C, Grand SP. 2018. Seismic attenuation in the African LLSVP estimated from PcS phases. *Earth Planet. Sci Lett.* 489:8–16

Lognonné P, Banerdt WB, Giardini D, Pike WT, Christensen U, et al. 2019. SEIS: Insight's seismic experiment for internal structure of Mars. *Space Sci. Rev.* 215(1):12

Lu C, Grand SP. 2016. The effect of subducting slabs in global shear wave tomography. *Geophys. J. Int.* 205(2):1074–85

Maguire R, Ritsema J, Bonnin M, van Keken PE, Goes S. 2018. Evaluating the resolution of deep mantle plumes in teleseismic traveltime tomography. *J. Geophys. Res. Solid Earth* 123:384–400

Maguire R, Ritsema J, van Keken PE, Goes S, Fichtner A. 2016. *P*- and *S*-wave delays caused by thermal plumes. *Geophys. J. Int.* 206:1169–78

Mancinelli N, Shearer P, Liu Q. 2016. Constraints on the heterogeneity spectrum of Earth's upper mantle. *J. Geophys. Res. Solid Earth* 121(5):3703–21

Marquering H, Nolet G, Dahlen FA. 1998. Three-dimensional waveform sensitivity kernels. *Geophys. J. Int.* 132:521–34

Marquering H, Snieder R. 1995. Surface wave mode coupling for efficient forward modeling and inversion of body wave phases. *Geophys. J. Int.* 120:186–208

Marra G, Clivati C, Luckett R, Tampellini A, Kronjäger J, et al. 2018. Ultrastable laser interferometry for earthquake detection with terrestrial and submarine cables. *Science* 361(6401):486–90

McNamara AK. 2019. A review of large low shear velocity provinces and ultra low velocity zones. *Tectonophysics* 760:199–220

McNamara AK, Zhong SJ. 2005. Thermochemical structures beneath Africa and the Pacific Ocean. *Nature* 437:1136–39

Meschede M, Romanowicz B. 2015. Lateral heterogeneity scales in regional and global upper mantle shear velocity models. *Geophys. J. Int.* 200(2):1076–93

Montelli R, Nolet G, Dahlen FA, Masters G. 2006. A catalogue of deep mantle plumes: new results from finite-frequency tomography. *Geochem. Geophys. Geosyst.* 7:Q11007

Montelli R, Nolet G, Dahlen FA, Masters G, Engdahl ER, Hung S-H. 2004. Finite-frequency tomography reveals a variety of plumes in the mantle. *Science* 303:338–43

Mosca I, Cobden L, Deuss A, Ritsema J, Trampert J. 2012. Seismic and mineralogical structures of the lower mantle from probabilistic tomography. *J. Geophys. Res.* 117(B6):B06304

Mosegaard K, Tarantola A. 1995. Monte Carlo sampling of solutions to inverse problems. *J. Geophys. Res.* 100(B7):12431–47

Moulik P, Ekström G. 2014. An anisotropic shear velocity model of the Earth's mantle using normal modes, body waves, surface waves and long-period waveforms. *Geophys. J. Int.* 199(3):1713–38

Moulik P, Ekström G. 2016. The relationships between large-scale variations in shear velocity, density, and compressional velocity in the Earth's mantle. *J. Geophys. Res. Solid Earth* 121:2737–71

Nakagawa T, Tackley PJ. 2004. Thermo-chemical structure in the mantle arising from a three-component convective system and implications for geochemistry. *Phys. Earth Planet. Int.* 146:125–38

Ni S, Ding X, Helmberger DV, Gurnis M. 1999. Low-velocity structure beneath Africa from forward modeling. *Earth Planet. Sci. Lett.* 170(4):497–507

Ni S, Tan E, Gurnis M, Helmberger D. 2002. Sharp sides to the African superplume. *Science* 296(5574):1850–52

Niu F, Levander A, Ham S, Obayashi M. 2005. Mapping the subducting Pacific slab beneath southwest Japan with Hi-net receiver functions. *Earth Planet. Sci. Lett.* 239:9–17

Nolet G, Hello Y, van der Lee S, Bonnieux S, Ruiz MC, et al. 2019. Imaging the Galápagos mantle plume with an unconventional application of floating seismometers. *Sci. Rep.* 9(1):1326

Obayashi M, Yoshimitsu J, Nolet G, Fukao Y, Shiobara H, et al. 2013. Finite frequency whole mantle *P* wave tomography: improvement of subducted slab images. *Geophys. Res. Lett.* 40:5652–57

Panning M, Capdeville Y, Romanowicz B. 2009. Seismic waveform modelling in a 3-D Earth using the Born approximation: potential shortcomings and a remedy. *Geophys. J. Int.* 177:161–78

Panning M, Lekić V, Romanowicz B. 2010. Importance of crustal corrections in the development of a new global model of radial anisotropy. *J. Geophys. Res.* 115(B12):B12325

Phạm T-S, Tkalčić H, Sambridge M, Kennett BLN. 2018. Earth's correlation wavefield: late coda correlation. *Geophys. Res. Lett.* 45:3035–42

Poli P, Campillo M, Pedersen H, LAPNET Work. Group. 2012. Body-wave imaging of Earth's mantle discontinuities from ambient seismic noise. *Science* 338(6110):1063–65

Rawlinson N, Spakman W. 2016. On the use of sensitivity tests in seismic tomography. *Geophys. J. Int.* 205(2):1221–43

Resovsky JS, Ritzwoller MH. 1999. Regularization uncertainty in density models estimated from normal mode data. *Geophys. Res. Lett.* 26:2319–22

Rickers F, Fichtner A, Trampert J. 2012. Imaging mantle plumes with instantaneous phase measurements of diffracted waves. *Geophys. J. Int.* 190:650–64

Rickers F, Fichtner A, Trampert J. 2013. The Iceland–Jan Mayen plume system and its impact on mantle dynamics in the North Atlantic region: evidence from full-waveform inversion. *Earth Planet. Sci. Lett.* 367:39–51

Ritsema J, Ni S, Helmberger DV, Crotwell HP. 1998. Anomalous shear velocity reductions and gradients in the lower mantle beneath Africa. *Geophys. Res. Lett.* 25:4245–48

Ritsema J, van Heijst HJ, Deuss A, Woodhouse JH. 2011. S40RTS: a degree-40 shear-velocity model for the mantle from new Rayleigh wave dispersion, teleseismic traveltime and normal-mode splitting function measurements. *Geophys. J. Int.* 184:1223–36

Ritsema J, van Heijst HJ, Woodhouse JH. 1999. Complex shear velocity structure imaged beneath Africa and Iceland. *Science* 286:1925–28

Romanowicz B. 2003. Global mantle tomography: progress status in the last 10 years. *Annu. Rev. Earth Planet. Sci.* 31:303–28

Romanowicz B, Gung Y. 2002. Superplumes from the core-mantle boundary to the lithosphere: implications for heat flux. *Science* 296(5567):513–16

Romanowicz B, Panning M, Gung Y, Capdeville Y. 2008. On the computation of long period seismograms in a 3D earth using normal mode based approximations. *Geophys. J. Int.* 175(2):520–36

Romanowicz B, Wenk H-R. 2017. Anisotropy in the deep Earth. *Phys. Earth Planet. Int.* 269:58–90

Rudolph ML, Lekić V, Lithgow-Bertelloni C. 2015. Viscosity jump in Earth's mid-mantle. *Science* 350(6266):1349–52

Sato H, Fehler MC, Maeda T. 2012. *Seismic Wave Propagation and Scattering in the Heterogeneous Earth*. Berlin: Springer-Verlag

Schaeffer AJ, Lebedev S. 2013. Global shear speed structure of the upper mantle and transition zone. *Geophys. J. Int.* 194:417–49

Shapiro NM, Ritzwoller MH. 2002. Monte-Carlo inversion for a global shear-velocity model of the crust and upper mantle. *Geophys. J. Int.* 151(1):88–105

Shephard GE, Matthews KJ, Hosseini K, Domeier M. 2017. On the consistency of seismically imaged lower mantle slabs. *Nat. Sci. Rep.* 7(1):10976

Shim SH. 2008. The postperovskite transition. *Annu. Rev. Earth Planet. Sci.* 36:569–99

Sigloch K, Mihalynuk MG. 2013. Intra-oceanic subduction shaped the assembly of Cordilleran North America. *Nature* 496:50–56

Simmons NA, Forte AM, Boschi L, Grand SP. 2010. GyPSuM: a joint tomographic model of mantle density and seismic wave speeds. *J. Geophys. Res.* 115(B12):B12310

Snieder R. 1986. 3-D linearized scattering of surface waves and a formalism for surface wave holography. *Geophys. J. Int.* 84:581–605

Spetzler J, Snieder R. 2001. The effects of small-scale heterogeneity on arrival time of waves. *Geophys. J. Int.* 144:786–96

Spica Z, Perton M, Beroza GC. 2017. Lateral heterogeneity imaged by small-aperture *ScS* retrieval from the ambient seismic field. *Geophys. Res. Lett.* 44:8276–84

Stixrude L, Jeanloz R. 2015. Constraints on seismic models from other disciplines—constraints from mineral physics on seismological models. In *Treatise on Geophysics*, ed. G Schubert, pp. 829–52. Amsterdam: Elsevier. 2nd ed.

Stockmann F, Cobden L, Deschamps F, Fichtner A, Thomas C. 2019. Investigating the seismic structure and visibility of dynamic plume models with seismic array methods. *Geophys. J. Int.* 219:S167–94

Styles E, Goes S, van Keken PE, Ritsema R, Smith H. 2011. Synthetic images of dynamically predicted plumes and comparison with a global tomographic model. *Earth Planet. Sci. Lett.* 311(3–4):351–63

Su WJ, Dziewoński AM. 1991. Predominance of long-wavelength heterogeneity in the mantle. *Nature* 352(6331):121–26

Suetsugu D, Shiobara H. 2014. Broadband ocean bottom seismology. *Annu. Rev. Earth Planet. Sci.* 42:27–43

Sun D, Tan E, Helmberger D, Gurnis M. 2007. Seismological support for the metastable superplume model, sharp features, and phase changes within the lower mantle. *PNAS* 104:9151–55

Tackley PJ. 2012. Dynamics and evolution of the deep mantle resulting from thermal, chemical, phase and melting effects. *Earth-Sci. Rev.* 110:1–25
Takeuchi N. 2007. Whole mantle SH velocity model constrained by waveform inversion based on three-dimensional Born kernels. *Geophys. J. Int.* 169(3):1153–63
Tanimoto T. 1995. Formalism for traveltime inversion with finite frequency effects. *Geophys. J. Int.* 121:103–10
Tape C, Liu Q, Maggi A, Tromp J. 2009. Adjoint tomography of the Southern California crust. *Science* 325:988–92
Tarantola A. 2005. *Inverse Problem Theory and Methods for Model Parameter Estimation*. Philadelphia: SIAM
To A, Fukao Y, Tsuboi S. 2011. Evidence for a thick and localized ultra low shear velocity zone at the base of the mantle beneath the central Pacific. *Phys. Earth Planet. Inter.* 184:119–33
Trampert J, Deschamps F, Resovsky J, Yuen D. 2004. Probabilistic tomography maps chemical heterogeneities throughout the lower mantle. *Science* 306(5697):853–56
Trampert J, Snieder R. 1996. Model estimations biased by truncated expansions: possible artifacts in seismic tomography. *Science* 271:1257–60
Tromp J, Tape C, Liu Q. 2005. Seismic tomography, adjoint methods, time reversal and banana-doughnut kernels. *Geophys. J. Int.* 160(1):195–216
van der Meer DG, van Hinsbergen DJJ, Spakman W. 2018. Atlas of the underworld: slab remnants in the mantle, their sinking history, and a new outlook on lower mantle viscosity. *Tectonophysics* 723:309–448
van der Voo R, Spakman W, Bijwaard H. 1999. Mesozoic subducted slabs under Siberia. *Nature* 397:246–49
Vance SD, Kedar S, Panning MP, Stähler SC, Bills BG, et al. 2018. Vital signs: seismology of icy ocean worlds. *Astrobiology* 18(1):37–53
Visser K, Trampert J, Kennett BLN. 2008. Global anisotropic phase velocity maps for higher mode Love and Rayleigh waves. *Geophys. J. Int.* 172(3):1016–32
Weber RC, Neal CR, Kedar S, Panning M, Schmerr NC, et al. 2018. Lunar seismology enabled by a deep space gateway. In *Deep Space Gateway Concept Science Workshop*, ed. B Bussey, JB Garvin, M New, P Niles, JF Spann, Pap. 3091. LPI Contrib. 2063. Houston: Lunar Planet. Inst.
Wen L. 2002. An SH hybrid method and shear velocity structures in the lowermost mantle beneath the Central Pacific and South Atlantic Oceans. *J. Geophys. Res.* 107(B3):ESE 4-1–4-20
White WM. 2015. Probing the Earth's deep interior through geochemistry. *Geochem. Perspect.* 4:95–251
Wolfe CJ, Solomon SC, Laske G, Collins JA, Detrick RS, et al. 2009. Mantle shear-wave velocity structure beneath the Hawaiian hot spot. *Science* 326:1388–90
Woodhouse JH, Dziewoński AM. 1984. Mapping the upper mantle: three-dimensional modeling of Earth structure by inversion of seismic waveforms. *J. Geophys. Res.* 89(B7):5953–86
Young A, Flament N, Maloney K, Williams S, Matthews K, et al. 2019. Global kinematics of tectonic plates and subduction zones since the late Paleozoic Era. *Geosci. Front.* 10(3):989–1013
Yu S, Garnero EJ. 2018. Ultra-low velocity zone locations: a global assessment. *Geochem. Geophys. Geosyst.* 19:396–414
Zhang Z, Dorfman SM, Labidi J, Zhang S, Li M, et al. 2016. Primordial metallic melt in the deep mantle. *Geophys. Res. Lett.* 43:3693–99
Zhao C, Garnero EJ, McNamara AK, Schmerr N, Carlson RW. 2015. Seismic evidence for a chemically distinct thermochemical reservoir in Earth's deep mantle beneath Hawaii. *Earth Planet. Sci. Lett.* 426:143–53
Zhao D. 2004. Global tomographic images of mantle plumes and subducting slabs: insight into deep Earth dynamics. *Phys. Earth Planet. Int.* 146(1–2):3–34
Zhou Y, Nolet G, Dahlen FA, Laske G. 2006. Global upper-mantle structure from finite-frequency surface-wave tomography. *J. Geophys. Res.* 111(B4):B04304
Zhu H, Bozdağ E, Peter D, Tromp J. 2012. Structure of the European upper mantle revealed by adjoint tomography. *Nat. Geosci.* 5:493–98

Annual Review
of Earth and
Planetary Sciences
Volume 48, 2020

Contents

In Pursuit
Inez Fung 1

Glacier Change and Paleoclimate Applications of Cosmogenic-Nuclide Exposure Dating
Greg Balco 21

The State of Stress on the Fault Before, During, and After a Major Earthquake
Emily E. Brodsky, James J. Mori, Louise Anderson, Frederick M. Chester, Marianne Conin, Eric M. Dunham, Nobu Eguchi, Patrick M. Fulton, Ryota Hino, Takehiro Hirose, Matt J. Ikari, Tsuyoshi Ishikawa, Tamara Jeppson, Yasuyuki Kano, James Kirkpatrick, Shuichi Kodaira, Weiren Lin, Yasuyuki Nakamura, Hannah S. Rabinowitz, Christine Regalla, Francesca Remitti, Christie Rowe, Demian M. Saffer, Saneatsu Saito, James Sample, Yoshinori Sanada, Heather M. Savage, Tianhaozhe Sun, Sean Toczko, Kohtaro Ujiie, Monica Wolfson-Schwehr, and Tao Yang 49

The Stratigraphy of Mass Extinctions and Recoveries
Steven M. Holland 75

Ab Initio Study on the Lower Mantle Minerals
Taku Tsuchiya, Jun Tsuchiya, Haruhiko Dekura, and Sebastian Ritterbex 99

Tsunami Modeling for the Deep Sea and Inside Focal Areas
Tatsuhiko Saito and Tatsuya Kubota 121

Mechanisms and Implications of Deep Earthquakes
Zhongwen Zhan 147

Slow Slip Events in New Zealand
Laura M. Wallace 175

The Geology and Biogeochemistry of Hydrocarbon Seeps
Samantha B. Joye 205

Advances in Cosmochemistry Enabled by Antarctic Meteorites
Meenakshi Wadhwa, Timothy J. McCoy, and Devin L. Schrader 233

Splendid Innovation: The Extinct South American Native Ungulates
Darin A. Croft, Javier N. Gelfo, and Guillermo M. López 259

Plate Tectonics and the Archean Earth
Michael Brown, Tim Johnson, and Nicholas J. Gardiner 291

Large Coseismic Slip to the Trench During the 2011 Tohoku-Oki Earthquake
Shuichi Kodaira, Toshiya Fujiwara, Gou Fujie, Yasuyuki Nakamura, and Toshiya Kanamatsu 321

Reconstructing Vertebrate Paleocolor
Jakob Vinther 345

Heterogeneity of Seismic Wave Velocity in Earth's Mantle
Jeroen Ritsema and Vedran Lekić 377

Ecological Response of Plankton to Environmental Change: Thresholds for Extinction
Christopher M. Lowery, Paul R. Bown, Andrew J. Fraass, and Pincelli M. Hull 403

Global Groundwater Sustainability, Resources, and Systems in the Anthropocene
Tom Gleeson, Mark Cuthbert, Grant Ferguson, and Debra Perrone 431

Jupiter's Interior as Revealed by Juno
David J. Stevenson 465

Trace Metal Substitution in Marine Phytoplankton
François M.M. Morel, Phoebe J. Lam, and Mak A. Saito 491

Climate Extremes and Compound Hazards in a Warming World
Amir AghaKouchak, Felicia Chiang, Laurie S. Huning, Charlotte A. Love, Iman Mallakpour, Omid Mazdiyasni, Hamed Moftakhari, Simon Michael Papalexiou, Elisa Ragno, and Mojtaba Sadegh 519

The Role of Diagenesis in Shaping the Geochemistry of the Marine Carbonate Record
Matthew S. Fantle, B. Davis Barnes, and Kimberly V. Lau 549

Dynamic Topography and Ice Age Paleoclimate
J.X. Mitrovica, J. Austermann, S. Coulson, J.R. Creveling, M.J. Hoggard, G.T. Jarvis, and F.D. Richards 585

Moist Heat Stress on a Hotter Earth
Jonathan R. Buzan and Matthew Huber 623

A Novel Approach to Carrying Capacity: From *a priori* Prescription to *a posteriori* Derivation Based on Underlying Mechanisms and Dynamics
Safa Mote, Jorge Rivas, and Eugenia Kalnay 657

Errata

An online log of corrections to *Annual Review of Earth and Planetary Sciences* articles may be found at http://www.annualreviews.org/errata/earth